THESIS FOR THE DEGREE OF DOCTOR OF PHILOSOPHY

Unveiling a multi-scale view of massive star and star cluster formation

CHI-YAN LAW

CHALMERS
UNIVERSITY OF TECHNOLOGY

Department of Space, Earth, and Environment
Chalmers University of Technology
Gothenburg, Sweden, 2024

Unveiling a multi-scale view of massive star and star cluster formation

CHI-YAN LAW

ISBN: 978-91-7905-829-6
Doktorsavhandlingar vid Chalmers tekniska högskola
Ny series nr 5449
ISSN 0346-718X
This thesis has been prepared using LaTeX.

Department of Space, Earth, and Environment
Chalmers University of Technology
SE-412 96 Gothenburg, Sweden
Phone: +46 (0)31 772 1000
www.chalmers.se

Printed by Chalmers Reproservice
Gothenburg, Sweden, Janurary 2024

Abstract

Massive stars regulate the physical and chemical evolution of galaxies. Most stars within these galaxies, including massive ones, appear to be born in star clusters. However, there are many open questions about how these systems form from diffuse interstellar gas. For example it is not yet known whether magnetic fields, turbulence or feedback are the most important actors in regulating gravitational collapse. It is also unclear to what extent potential protostellar crowding within a protocluster may affect massive star formation. Thus it is important to measure levels of turbulence and magnetic fields in star-forming clouds to test theoretical formation models. On the smaller scales of individual massive star formation, various theories, including core accretion, competitive accretion and protostellar collisions, may be viable depending on environmental conditions. Hence, studying how massive stars are forming in environments with relatively extreme conditions, e.g., in terms of crowding or isolation, may yield the most stringent constraints on these models. Studying the variation of star formation properties with galactic environment, e.g., metallicity, is also an important goal for helping to develop the most general theoretical understanding of star formation.

We first present a study of a massive protostar (G28.2-0.05) that appears to be forming in relative isolation. Observational data, especially from the Atacama Large Millimeter/Submillimeter Array (ALMA), are used to investigate the nature of the system, including its dense and ionized gas structures, small-scale kinematics and dynamics and large-scale outflows. Mid to Far Infrared observations and archival data are used to measure the spectral energy distribution (SED) to further constrain protostellar properties. We conclude the system is a massive ($\sim 40\ M_{\odot}$) protostar that has an accretion powered wide angle bipolar molecular outflow and is also in the first stages of producing significant ionizing feedback. An examination of the mm dust continuum emission in the surroundings finds a near complete dearth of other sources, which is evidence for the system's isolation and a strong constraint on competitive accretion models. Overall, core accretion models appear to give a good description of the protostar. Follow-up studies have measured the astrochemical content of the protostellar envelope and will help guide future chemodynamical models of massive star formation.

We next present the first results of an observational survey Polarised Light from Massive Protoclusters (POLIMAP), which studies the magneto-kinematic

properties of a sample of infrared dark clouds (IRDCs) using SOFIA-HAWC+ observations, complemented by GBT-Argus observations of ^{13}CO and C^{18}O line emission. We present POLIMAP results for the massive IRDC G28.37+0.07. We show that magnetic fields are playing an important role in this IRDC, i.e., during the early stages of massive star and star cluster formation.

Finally, we present a study of the Galactic carbon isotope abundance gradient derived from observations of the species H_2CO and HC_3N from a large sample of 100 massive star-forming clumps across the Galaxy, observed as part of the ALMAGAL survey. We find an average ratio of ^{12}C to ^{13}C of 30, which is relatively low compared to previous studies. Our measurements also show a large scatter of 1.7 dex. We propose that these results can be explained by the effects of optical depth in the ^{12}C lines of HC_3N and H_2CO leading to systematic biases in the measurements. We quantify the impact of optical depth with a combination of single dish and interferometric data, which for a handful of sources show that the ratio of of ^{12}C to ^{13}C could increase by a factor of 2-3. Hence, we argue that multi-transition analysis is required to accurately correct for optical depth effects to obtain accurate isotopic ratios.

Keywords: ISM:clouds, stars:formation, magnetic field, massive stars, methods:observation

List of Publications

This thesis is based on the following publications:

[A] **Chi-Yan Law**, Jonathan C. Tan, Prasanta Gorai, Yichen Zhang, Rubén Fedriani, Daniel Tafoya, Kei Tanaka, Giuliana Cosentino and Yao-Lun Yang. , "Isolated Massive Star Formation in G28.20-0.05". *ApJ*, vol. 939, 2022. doi:10.3847/1538-4357/ac90c7.

[B] **Chi-Yan Law**, Jonathan C. Tan, Raphael Skalidis, Duo Xu, Larry Morgan, Giuliana Cosentino, Chia-Jung Hsu, Ruben Fedriani, "Polarized Light from Massive Protoclusters (POLIMAP). I.
Dissecting the role of magnetic fields in the massive infrared dark cloud G28.37+0.07". Manuscript in preparation.

[C] **Chi-Yan Law**, M. T. Beltrán, Leonardo Testi, Chiara Minnini, Jonathan C. Tan, and ALMAGAL consortium, "Uncovering the carbon isotopologue gradient in the Milky Way". Manuscript intended for submission to A&A.

Other publications by the author, not included in this thesis, are:

[D] Duo Xu, **Chi-Yan Law**, Jonathan C. Tan, "Application of Convolutional Neural Networks to Predict Magnetic Fields Directions in Turbulent Clouds". *ApJ*, vol. 942, 2023. doi:10.3847/1538-4357/aca66c.

[E] Prasanta Gorai, **Chi-Yan Law**, Jonathan C. Tan, et al., "Astrochemical Diagnostics of the Isolated Massive Protostar G28.20-0.05". Accepted for publication in *Astrophysical Journal*.

Acknowledgments

First and foremost, I want to thank my supervisor, Jonathan Tan, for his guidance, support and patience during my PhD. He gave me a unique chance to study massive star formation in Sweden and work with many amazing collaborators. I also thank him for really giving me the experience of what is meant to be an independent researcher, in both attitude and also the skills to work on my Ph.D. projects. I also thank Jouni Kainulainen for being my second supervisor, and for providing suggestions and valuable advice in navigating a research career or on the attitude in conducting research. I would also want to thank Leonardo Testi for being my supervisor during my stay at ESO and with all the guidance on the ALMAGAL project. I also want to thank Wouter Vlemmings for being my examiner, Vincent Desmaris for being my study leader, and Matthias Maercker for being an amazing line manager. I can feel your care for my mental health. I would especially like to thank Prasanta Gorai, Giuliana Cosentino, Rubén Fedriani, Juan Farias, and Yichen Zhang for hearing me out on many things, on and off research, and being patient with me in providing helpful feedback on my research and writing. I also want to thank Daniel Tafoya, Maria Carmen Toribio and the Nordic ALMA arcnode staff for the great help during long and painful ALMA data reduction and understanding the ALMA data. I also want to thank Jasmine Nilsson for helping deal with much paperwork.

It is my honour to meet a lot of amazing colleagues at Chalmers and Onsala Space Observatory, who have helped me out a lot throughout my Ph.D. I would first sincerely thank Andri Spilker, Chia-Jung Hsu, Kyoko Onishi, Sara Piras, Sandra Treviño Morales and Mamiko Sato. I cannot imagine what my Ph.D. life would be like without you guys, even though I know I am really bad at communication! I am also really grateful to have met Iskra Georgieva, Kiana Kade, Jan Orkisz, Sara Rezaei Kh. and many others. My Ph.D. life becomes lively with you guys around!

Finally and most importantly, I would want to give a huge thanks to my family in Hong Kong for their great support in all the ups and downs! I also want to thank all the brothers and sisters in Christ near and far (NCCC Göteborg, Kwan's, CFC (youth), Boys, Elpida/Aliya, research cell, and more).

Contents

Part I

Scientific context

CHAPTER 1

Introduction

Stars are the main visible, baryonic component of the Milky Way and most other galaxies. Depending on their mass, stars will evolve to different outcomes (see Fig. 1.1), with 'massive' or 'high-mass' stars typically defined as those that start their lives with eight solar masses or more. While massive stars are a relatively small fraction of the total stellar mass, they dominate radiative, mechanical and chemical feedback on the ISM and galaxies, including via the regulation of further star formation. For instance, at very early stages, forming massive protostars may shape the physical conditions of any surrounding protocluster by radiative heating and mechanical feedback from outflows. Eventually, stellar winds and ionizing feedback from fully formed massive stars are likely to be the main agents that disperse remnant molecular gas halting further star formation in the vicinity. Massive stars are responsible for the nucleosynthesis of a large fraction of chemical elements including Carbon, Nitrogen, Oxygen, including their various ispotopologues. In this way the nucleosynthetic yields from supernovae help to control galactic chemical evolution e.g., Kobayashi et al., 2011; Romano et al., 2019.

Thus, we see that massive stars are an essential process for the life cycle of the interstellar medium and galaxies (Tinsley, 1980; Zinnecker & Yorke, 2007;

Tan et al., 2014; Romano, 2022). However, the formation process of massive stars remains shrouded in uncertainty and warrants further investigation. For example, the relative importance of magnetic fields, turbulence, and feedback (e.g., outflows/jets, radiation pressure, ionization) in mediating gravitation collapse remains uncertain (e.g., Tan et al., 2014; Motte et al., 2017; Rosen et al., 2020). It is also unclear how the initial conditions of molecular clouds before collapse impact on the eventual massive star and star cluster formation. Furthermore, whether clustering of stars is essential for the formation of individual massive stars or if it is also possible to form them from isolated cores is an open question. It is also unclear if the chemical conditions of star and planet-forming regions inherit certain characteristics from the large-scale galactic environment or are reset due to local chemical evolutionary processes (Gonzalez et al., 2001; Pontoppidan & Blevins, 2014). To answer these questions, observations provide crucial information to test theories of massive star and star cluster formation. Hence, the overall goal of this thesis is to advance our understanding the processes of massive star and star cluster formation by such observational tests.

The outline of this thesis is as follows. In the remaining part of Chapter 1, we describe the main evolutionary stages of massive star formation and discuss the open questions to be addressed in this thesis. In Chapter 2, we discuss the physical processes involved in massive star and star cluster formation. The environments of massive star and star cluster formation are GMCs, which are typically defined as having masses $> 10^4\ M_\odot$, and especially their densest clumps, which in early stages are often observed as Infrared Dark Clouds (IRDCs). Observational studies of gas motions in GMCs and IRDCs suggest that they are supersonically turbulent. However, polarimetric studies toward these clouds often indicate the presence of a relatively ordered magnetic field morphology, which indicates that magnetic fields also play a role in regulating the large-scale environment of star formation. As we discuss in later parts of this thesis, the different environmental conditions of GMCs and their dense star forming clumps, i.e., with greater levels of turbulent and magnetic pressures, are expected to be important for the overall processes of massive star and star cluster formation. In Chapter 3, we review the different observational methods that we have used to study massive star and star cluster formation. Most of the focus is on the use of radio and infrared telescopes to gain information about the properties of gas and dust in GMCs, IRDCs,

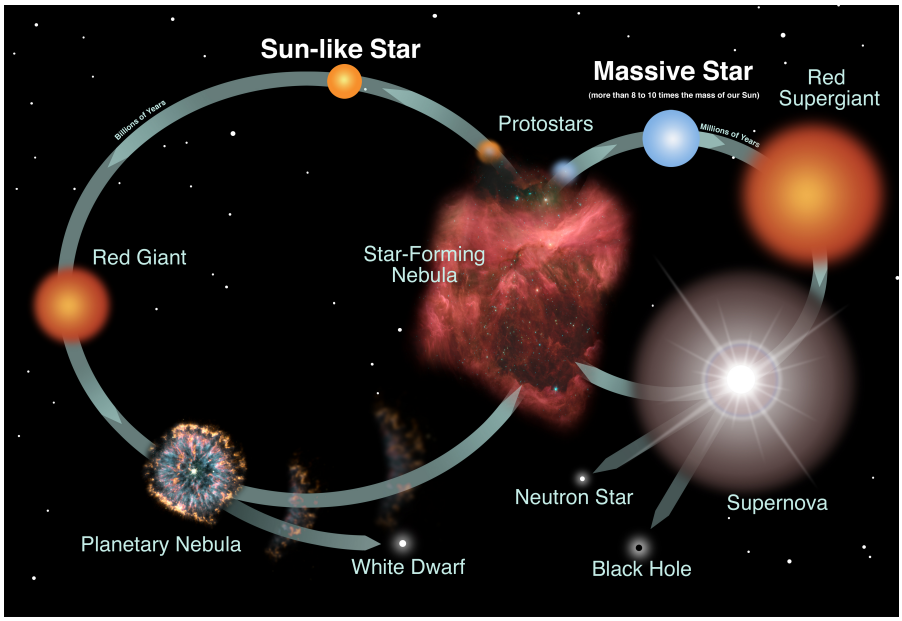

Figure 1.1: Schematic diagram summarizing the main stages of the life cycle of low-mass, Sun-like stars and massive stars. (Image credit: NASA and Night Sky Network).

cores and outflows. Furthermore, the main method we use to study magnetic fields involves studying polarized dust emission that is expected to arise from magnetically-aligned elongated dust grains. In Chapter 4, we provide a summary of each of the papers and the data used in each work.

1.1 The Evolutionary Stages of Massive Star and Star Cluster Formation

Overview of Core Accretion of Low-Mass Stars

While this thesis will focus on the formation of massive stars and star clusters, it is first useful to provide a summary of the main stages of isolated low-mass star formation, since this forms the basis of one of the main classes of massive

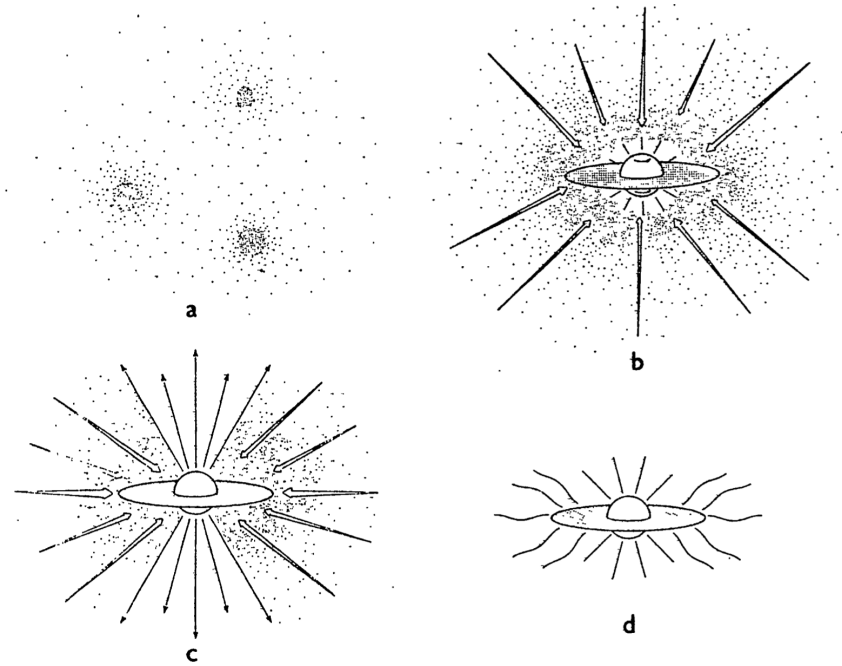

Figure 1.2: A schematic diagram illustrating the major stages of low-mass star formation adopted from Shu et al. (1987). Within the dense part of the molecular cloud ('clump') where gravity develops and dominate over turbulence and magnetic fields collapse led to the formation of dense cores. Within the cores, protostars are born, each fed by a rotating disk and collapsing envelope. The disks launch bipolar outflows that disperse the remaining core gas to reveal a pre-main sequence T-Tauri star, which can still retain a circumstellar disk.

star formation theories, i.e., core accretion. Figure 1.2 presents an schematic diagram of low-mass star formation (Shu et al., 1987). In cold ($\sim$ 10 K), dense regions in molecular clouds, i.e., where H is mainly in molecular form, gravitational instabilities develop, leading to the emergence of prestellar cores (PSCs). These cores are self-gravitating, centrally concentrated, and exhibit infall motions. When conditions become optically thick in the center of a PSC, internal pressure builds up leading to support against gravitational collapse and formation of a first hydrostatic core, which is still composed of molecular hydrogen. When the temperature is high enough that molecular hydrogen is dissociated, further gravitation collapse occurs, forming a quasi-hydrostatic protostar and the system is then referred to as a protostellar core. Accretion continues from the envelope to the protostar. Infalling gas can retain some angular momentum of the larger-scale core envelope, leading to the formation of a rotationally supported accretion disk. Associated with this disk is the launching of accretion powered bipolar protostellar outflows, with collimation mediated by magnetic fields that are coupled to the disk. The outflow begins to clear the surrounding envelope gas above and below the disk creating low-density outflow cavities. The overall efficiency of star formation from a core due to outflow feedback is expected to be $\sim 30-50\%$. Most low-mass stars are now known to form planetary systems that formed from the remnant accretion disk. Eventually, on timescales up to $\sim$ 10 Myr, the disk has largely dissipated and the pre-main sequence star is full revealed. It should be noted, that there remain many open questions concerning low-mass star formation, such as the role of turbulence and magnetic fields in mediating collapse, disk formation and outflow launching, the rate of evolution of dust grains in the core and the timescale of the onset of planet formation.

Infrared Dark Clouds (IRDCs)

Infrared Dark Clouds (IRDCs) are cold, dense regions shadowing the diffuse Galactic mid-infrared (MIR) background. They are typically found in Giant Molecular Clouds (GMCs) and are likely to be the precursors of massive stars and star clusters (Perault et al., 1996; Egan et al., 1998; Simon et al., 2006). Figure 1.3 shows three well studied IRDCs exhibited as such dark silhouettes in front of the mid-infrared Galactic emission as observed with the Spitzer Space Telescope (Barnes et al., 2021).

Many IRDCs appear to be globally filamentary or to contain filamentary

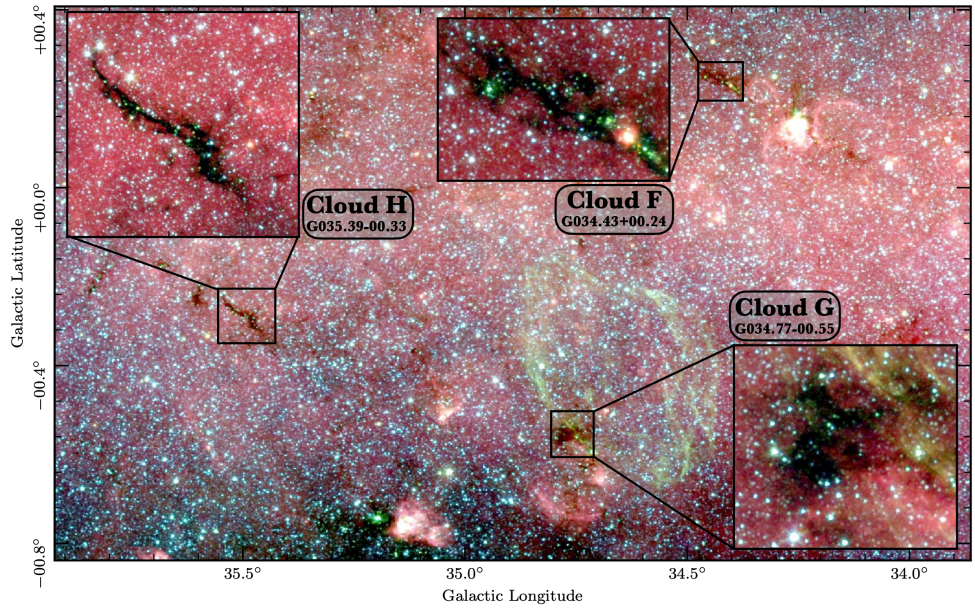

Figure 1.3: (From Barnes et al., 2021): Three-color image of part of the Galactic plane which highlights several infrared dark clouds (IRDCs). In this image, red is 8 μm, green is 5.8 μm and blue is 4.5 μm emission from the Spitzer GLIMPSE survey (Carey et al., 2009). The three IRDCs are Clouds F (G34.43+0.24), G (G34.77-0.55), and H (G35.39-0.33) following the naming in Butler & Tan (2009). The inset panels show zoom-ins of these IRDCs.

sub-structures (e.g., Butler & Tan, 2012). Such filaments may arise due to local turbulent shock compression within GMCs, collisions between GMCs (e.g., Wu et al., 2018), compression in feedback shells (e.g., Cosentino et al., 2020), collision of feedback shells with each other (e.g., Inutsuka et al., 2015), magnetically regulated collapse (e.g., Li et al., 2014), or some combination of these processes.

Numerous studies have been carried out to characterize the physical conditions of IRDCs (e.g., Rathborne et al., 2006; Butler & Tan, 2009; Butler & Tan, 2012; Kainulainen & Tan, 2013; Hernandez & Tan, 2015; Sokolov et al., 2017). Figure 1.4 shows the dust extinction map of Cloud H (G35.39-00.33)

from Kainulainen & Tan (2013). The extinction map is constructed by combining mid-infrared and near-infrared extinction data. The high extinction up to at least $A_V \sim 100$ mag indicates high column densities ($N_{\rm H} \sim 1.87 \times 10^{23}$ cm^{-2} assuming a conversion factor of $N_{\rm H}/A_V = 1.87 \times 10^{21}$ (cm^{-2}/mag) (Bohlin et al., 1978). Based on such column density maps, estimates of the volume densities can be made, with values of $n_{\rm H} \sim 10^{3-6}$ cm^{-3} inferred for structures with masses in the range $\sim 10^5$ down to 10 $M_\odot$ (Butler & Tan, 2012). Temperatures in IRDCs have been measured from studies of NH_3 emission (Pillai et al., 2015) and from FIR dust SEDs (Lim et al., 2016), with values of ~ 15 K inferred. Pillai et al. (2015) (see also Soam et al., 2019; Tang et al., 2019) mapped the plane of sky magnetic fields using polarized dust continuum emission toward two IRDCs and, via the DCF method, inferred the presence of dynamically strong, ∼mG $B-$fields and sub-Alfvénic turbulence $M_A \sim 0.5$. This strong field strength would be sufficient to support the formation and evolution of relatively massive and dense cores (Tan et al., 2013).

Fragmentation of IRDCs into Prestellar Cores

Different theoretical models for massive star and star cluster formation make different predictions for how fragmentation proceeds in molecular clouds. Thus studying the fragmentation process in IRDCs is an important goal to test these models.

The two major models of massive star formation are core accretion (e.g., McKee & Tan, 2003) and competitive accretion (Bonnell et al., 2001). The core accretion model (see Figure 1.5) proposes that massive stars form by a process that is a scaled-up version of the low-mass star formation model (Shu et al., 1987), thus the formation of a massive star happens from material localized in a well-defined region, i.e., the dense core. However, in the turbulent core model of McKee & Tan (2003) massive cores are mostly supported by a combination of turbulence and magnetic fields (e.g., Butler & Tan, 2012; Tan et al., 2014), i.e., to be in a state of near virial equilibrium and to prevent fragmentation. For typical massive cores seen in IRDCs and assuming equipartition of turbulent and magnetic energies, ∼ mG magnetic field strengths are predicted to be present (Butler & Tan, 2012). The turbulent core model also predicts a relatively more disordered collapse of the dense core compared to low-mass, thermally supported cores, due to its turbulent

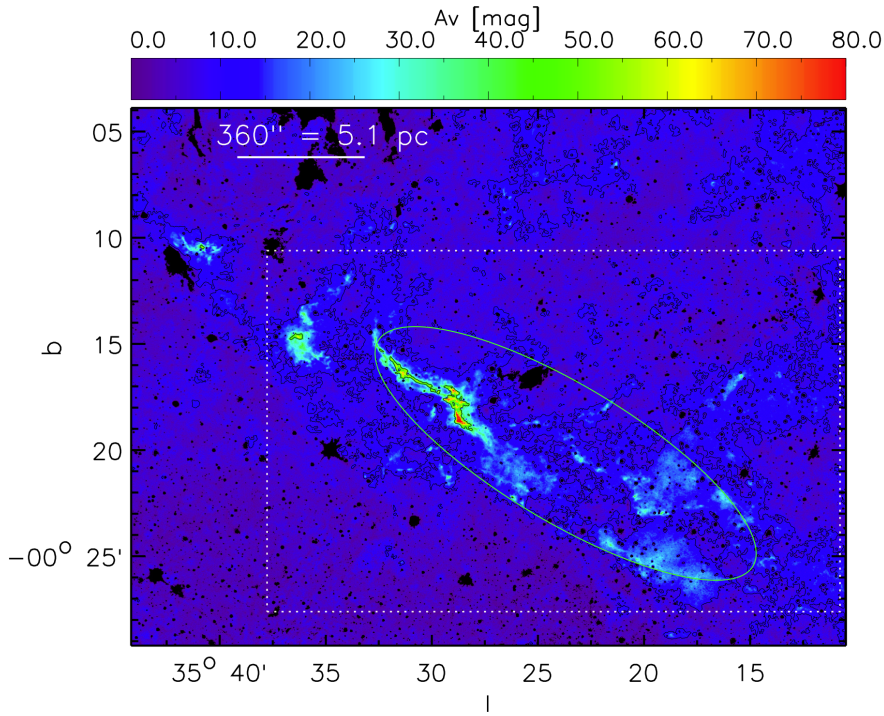

Figure 1.4: Dust extinction map of Cloud H (G35.39-00.33) constructed from mid-infrared and near-infrared data (Kainulainen & Tan, 2013).

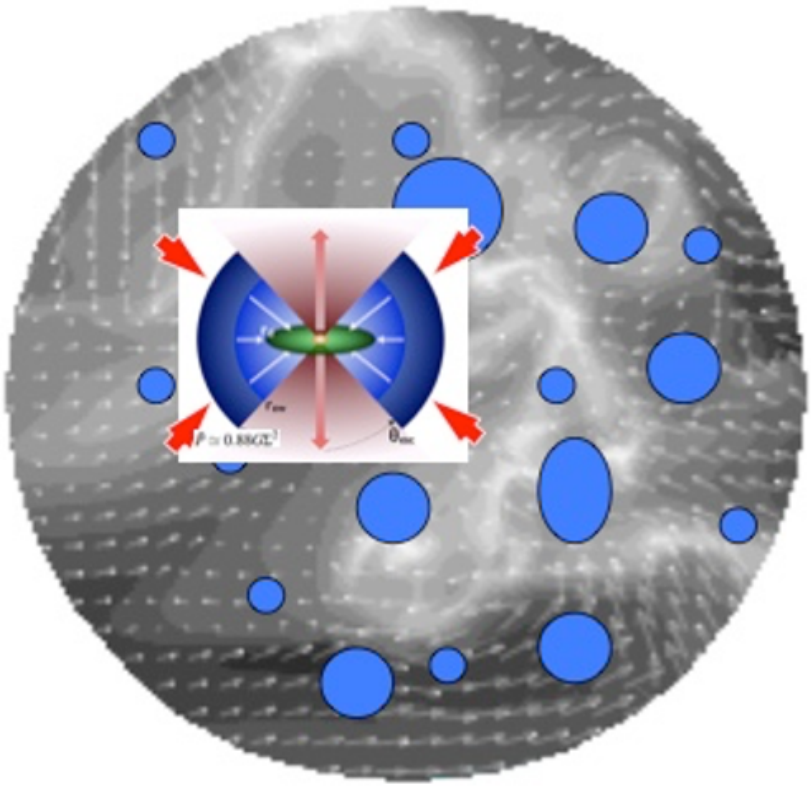

Figure 1.5: A schematic diagram showing the core accretion model. (image credit: Jonathan Tan).

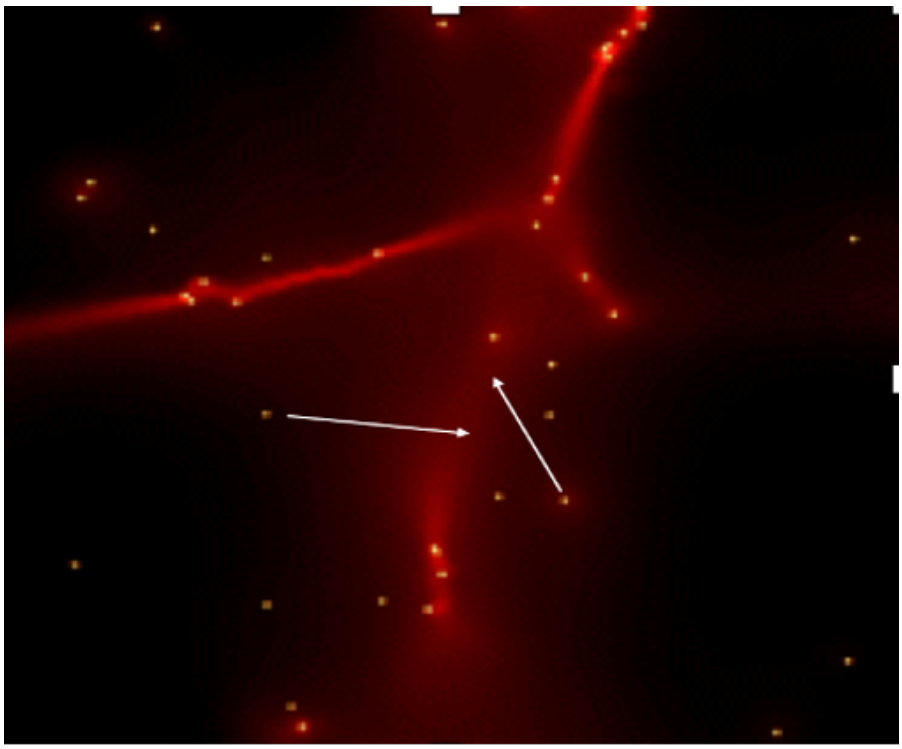

Figure 1.6: A schematic diagram of competitive accretion model (image credit: Bonnell et al. (2001)).

nature, perhaps including significant accretion via over-dense filaments and other sub-structures, e.g., as seen in magnetohydrodynamical (MHD) simulations of such structures (Seifried et al., 2012; Myers et al., 2013; Hsu et al., 2021).

One feature of core accretion models is that it is expected to be relatively easy for them to overcome the radiation pressure feedback problem of massive star formation (see, e.g., Tan et al., 2014). This is because the material starts in a dense core configuration, which then forms an optically thick accretion disk allowing material to reach the central source. The radiative feedback from the protostars is efficiently channelled in to the protostellar outflow cavities, i.e., the flashlight effect, and thus is not effective at halting accretion.

In the Competitive Accretion model (see Figure 1.6), stars chaotically gain their mass via the global collapse of the clump without passing through the massive pre-stellar core phase. This model predicts that massive stars always form in clustered environments, i.e., surrounded by many lower-mass protostars. The massive starts tend to take relatively long timescales to form, i.e., $\gtrsim 1$ Myr, i.e., on the timescale of global collapse of the clump. They then tend to form later than most other stars in the cluster. Disks around massive protostars are generally expected to be smaller than in core accretion models due to tidal disruption from surrounding lower-mass stars. The orientation of the disk is expected to change many times over the duration of accretion given that the infalling material is not from a coherent core and because of the strong dynamical interactions with surrounding lower-mass stars.

Massive protostellar cores / hot molecular cores

Massive protostars, being sources of high luminosity and surrounded by large quantities of dense gas, lead to astrochemically rich conditions, observed as "hot molecular cores" (HMCs). These cores are characterized by being compact (≤ 0.1 pc), warm ($T > 100$ K), and dense ($n_{\rm H} > 10^6$ cm^{-3}) (e.g., van der Tak, 2004; Beuther, 2007; Tan et al., 2014).

Examples of a radio spectra toward two HMCs are presented in Figure 1.7 (Beuther et al., 2007a; Beuther et al., 2007b). Many complex organic molecules (COMs) have been identified in such spectra, including species that are building blocks of prebiotic molecules, such as amino acids and proteins (e.g., Chakrabarti & Chakrabarti, 2000; Garrod, 2013).

Following the cold IRDC and pre-stellar core phases, molecules are mostly

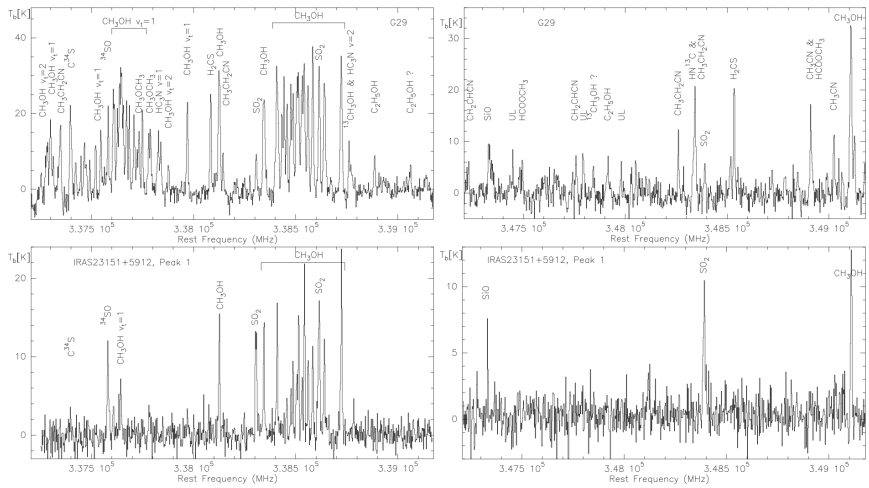

Figure 1.7: SMA spectra adopted from Beuther et al. (2007a) and Beuther et al. (2007b) toward two massive star-forming regions (Top: G29.96; Bottom: IRAS 23151+5912). The spectra show forests of emission lines from a great variety of simple and complex species.

frozen onto dust grains. The HMC phase involves these species being thermally desorbed into the gas phase. Chemical processing can occur both in the ice before desorption and in the gas phase. Furthermore, the local chemical evolutionary process happening in the hot molecular core and in the HII region (see next section) could significantly modify the initial chemical condition, causing a reset in the chemical conditions in the local star and planet-forming regions.

The massive protostar G28.2-0.05 that is studied in this thesis has been revealed to be one of the most chemically rich sources (Gorai et al., 2023). The physical characterization of the source we have carried out will be important for the astrochemical modeling of this source.

Ionizing feedback as traced by HII regions

HII regions are the locations where H is ionized (Hoare et al., 2007). Young massive stars produce high quantities of extreme ultraviolet (EUV) photons that efficiently photoionize the gas around them. Gas may also be ionized by strong shocks, e.g., driven by protostellar outflows and stellar winds. Photoionized gas reaches temperatures of about 10,000 K and so is overpressured compared to surrounding molecular cloud gas (Churchwell, 2002; Hoare et al., 2007). Thus HII regions begin to expand into their surroundings and this may be a crucial feedback process that destroys molecular clouds (e.g., Kirsanova et al., 2008; Devaraj et al., 2021).

As an example, Figure 1.8 presents an image of the HII region Sh2-284, which is powered by photoionization from already-formed massive stars. These HII regions are among the brightest objects in the mid-infrared to radio wavelengths (Hoare et al., 2007; Churchwell, 2002).

Owing to such high luminosity, HII regions are targeted by observers as the "signpost" for recently formed massive stars. To date, over 2,000 HII regions have been detected across the Galaxy, including using MIR survey data, followed up by studies of cm radio continuum free-free emission (Wenger et al., 2021).

During the earlier protostellar phase, HII regions are smaller and indeed are characterized via their size, i.e., Hyper-Compact (HC) HII regions (< 0.01 pc) and Ultra-Compact (UC) HII regions (Churchwell, 2002). Large samples of UC HII regions were first characterized by Wood & Churchwell (1989) based on IRAS data. Some examples of UC-HII regions in radio wavelengths are presented in Figure 1.9, which display different basic morphologies. For instance, G28.2-0.05, the source analysed in this project, is a shell-like HC-HII region (Sewiło et al., 2008). The different morphologies could potentially be important in understanding the evolution of the massive star-forming environments, as they may retain memory on the gas structures present before ionization (Churchwell, 2002).

The radio spectral energy distribution (SED) of an HII region typically has a shape presented in Figure 1.10. The spectral break corresponds to the frequency when optical depth $\tau \sim 1$ Condon & Ransom (2016) . At frequencies lower than the break, where $\tau > 1$, the SED follows a black body with spectral index $\alpha_\nu \simeq 2$, where $S_\nu \propto \nu^{\alpha_\nu}$. On the optically thin side, the optically thin free-free emission results in a characteristic spectral index

Figure 1.8: Four color image of the HII region Sh2-284 as seen by WISE. Blue and cyan correspond to emission at 3.4 and 4.6 μm, while green and red show emission at 12 and 22 μm, respectively. Credit: NASA/JPL-Caltech/UCLA

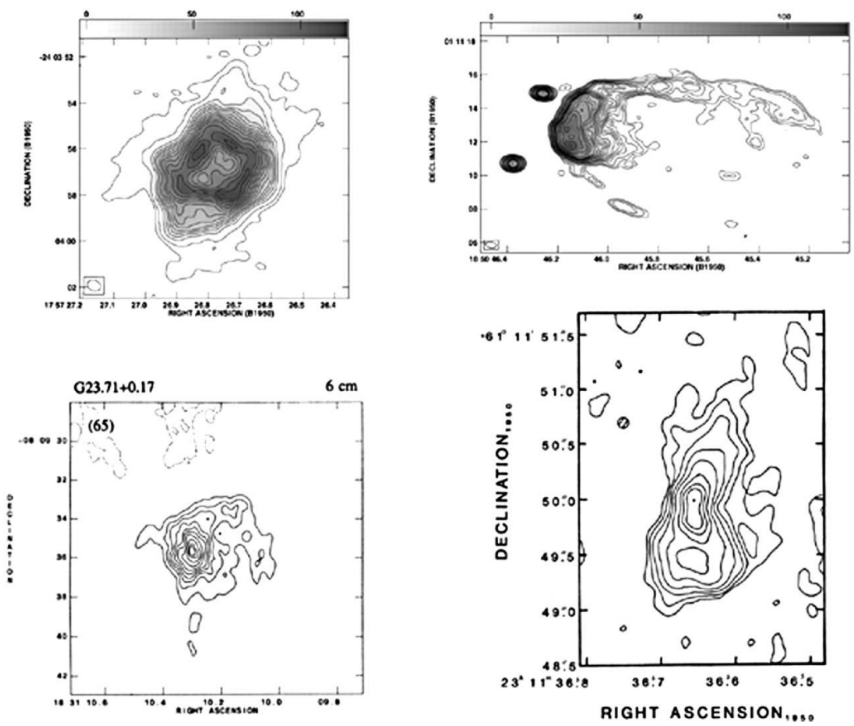

Figure 1.9: Examples of UC-HII regions with different morphologies: Shell-like (top left), Cometary (top right), Core-halo (bottom left), Bipolar (bottom right). Figure is adapted from Rodríguez (2005).

of $\alpha_\nu \simeq -0.1$ Condon & Ransom (2016). However, the radio SED of an HII region can involve a more intermediate power law index over a broader range of frequencies if there is an underlying density structure in the HII region, e.g., as in that of a stellar wind or protostellar outflow (e.g., Tanaka et al., 2017). The radio emission from HCHII regions can be a crucial diagnostic to help pinpoint the location of massive protostars that are just starting to ionize their local environments.

1.2 Open questions in massive star and star cluster formation

After reviewing key stages of massive star and star cluster formation, one realises that these are complex dynamical processes, with many outstanding open questions. In the following, we discuss three questions that are related to this thesis: (i) What is the relation of massive star formation to star cluster formation? (ii) Do mass stars form as scaled-up version of low-mass star formation?; and (iii) To what extent do the physical and chemical conditions of star/planet-forming regions depend on Galactic environment? Answering these questions will make significant steps forward to understanding how massive stars and star clusters form.

1. What is the relation of massive star formation to star cluster formation?

This question can be also be expressed as: can massive stars form in isolation or do they require the presence of a star cluster; and, when forming in a cluster, do massive stars tend to form in the center (i.e., is there primordial mass segregation)? Observationally there are some claims that massive stars tend to be found in the centers of rich star clusters (e.g., Hillenbrand & Hartmann, 1998; Kirk & Myers, 2011). On the other hand, Moser et al. (2019) did not find evidence for primordial mass segregation from an analysis of 35 high and intermediate mass protostars in IRDC G28.37. Whether or not they are born in the central regions, i.e., with primordial mass segregation, or whether their central concentration is due to subsequent dynamical evolution in a cluster, i.e., after the massive star has formed, provides important constraints on formation theories (e.g., Bonnell & Bate, 2006).

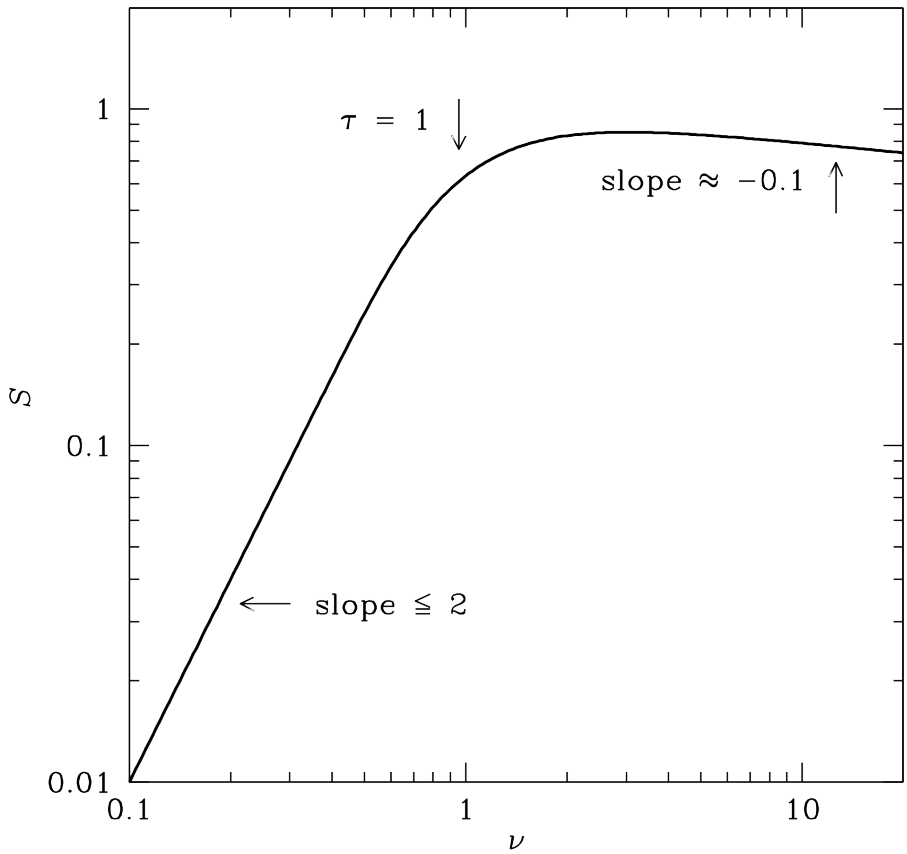

Figure 1.10: The typical shape of the spectral energy distribution of HII regions. The slope at a frequency below the spectral break, indicated at the frequency when $\tau = 1$ is optically thick and follows a black body. The drop follows an index of ~ 2 assuming a cylindrical geometry. For the frequency higher than the spectral break, the slope index is -1, which is correlated with the electron density. Figure from Condon & Ransom (2016).

Observational studies on the magnetic field and turbulent properties in IRDCs will be able to constrain the properties of star cluster formation and also provide insight on the link of larger scale environment of star cluster formation on massive star formation. For instance, the study by Seifried & Walch (2015) suggested that the magnetic field orientation may have an effect on the resulting properties of star clusters. In fact, bimodal cloud-field orientation is observed in the massive infrared dark cloud G28.37+0.07 (Chapter 4), placing constraints on the initial conditions of star cluster formation.

2. Do massive stars form via core accretion or competitive accretion?

Several observational features may provide important information to help distinguish between core and competitive accretion: (1) Core mass function; (2) Identification of massive dense cores, including pre-stellar cores; (3) Existence of massive protostars in relatively isolated regions; (4) Characterisation of outflow and disk properties in massive protostars.

(1) Core mass function: A characteristic feature of core accretion models is a more direct linkage of the pre-stellar core mass function (CMF) and the stellar initial mass function (IMF). Several observational studies have found CMFs shapes that are similar to that of the IMF (e.g., Alves et al., 2007; André et al., 2010; Könyves et al., 2015; Cheng et al., 2018). On the other hand, in the competitive accretion framework, there is no correlation between the CMF and the IMF as the accretion involves randomly fed ambient gas materials from the clump or the parent cloud (e.g., Padoan et al., 2020).

(2) Identification of massive dense cores, including pre-stellar cores: Another important observational feature to disentangle between the two scenarios is to look for massive dense cores, especially pre-stellar cores. For instance, some CMF studies (e.g., Motte et al., 2018; Liu et al., 2018; O'Neill et al., 2021) have found relatively shallow CMF indices, suggesting the existence of massive dense cores. Furthermore, ALMA observations toward IRDC G28.37+0.07 by Tan et al. (2013) identified two massive dense prestellar core candidates with masses as high as $60 M_{\odot}$. Csengeri et al. (2017) surveyed 35 sources with ALMA and found that most of them show limited fragmentation, with at most 3 cores per clump. On the other hand, some observations find higher levels of fragmentation: e.g., Cyganowski et al. (2017) studied the high-mass star-forming region G11.92-0.61 finding that the three

massive protostars in the region are surrounded by at least 16 lower mass protostellar sources within a region about 0.3 pc in radius; Sanhueza et al. (2019) studied 12 IRDCs clumps and revealed a higher level of fragmentation with a large population of low-mass cores with sizes smaller than 0.1 pc, but no high-mass counterparts.

(3) Massive protostars in isolated environments: A main observational prediction of competitive accretion models is that massive stars must form in crowded environments. Hence, the identification of massive stars forming in relatively isolated environments would provide evidence in favour of core accretion, at least in these regions. G28.2-0.05, the massive protostellar system analyzed in this thesis provides a case study for this type of investigation.

(4) Characterization of outflow and disks of massive protostars: An important feature of the core accretion model, as a scaled-up version of low-mass star formation, is that there is similar governing physics, but with more powerful outflows (given that the accretion power is stronger) and with more massive disks (e.g., if the disk mass is a fixed fraction of the central stellar mass). Furthermore, a dynamically important magnetic field may be expected to support massive dense cores from fragmentation. In fact, the magnetic field has been shown to play an important role in regulating disk size and outflow collimation (Bally, 2016; Commerçon et al., 2022). The outflow in G28.2-0.05 is found to be aligned close to normal to the inferred rotation axis of the massive protostellar disk.

It is also noted that the relative importance of magnetic fields is key to testing different models. Hence, multi-wavelength studies of cloud-to-disk scale will provide a comprehensive view of the role of magnetic fields in massive star and star cluster formation.

3. To what extent do the physical and chemical conditions of star/planet-forming regions depend on Galactic environment?

The physical and chemical conditions of massive protostars under dramatic changes during the evolution of the core from pre-stellar conditions to the hot molecular core and ultra-compact HII region phases. In particular, the thermal heating from the massive protostar unlocks great varieties of chemical species from dust to gas. Direct photo-dissociation and ionization feedback further affects physical and chemical evolution. In fact, G28.2-0.05 has been

demonstrated by Gorai et al. (2023) to be very chemically rich.

Studying how physical and chemical processes change with Galactic environment is of general importance to help constrain theoretical models. The first step in this process is to construct a sample of massive protostars that span a range of environments. In this thesis, we have carried out analysis of such a sample from the ALMAGAL survey. Our analysis, part of the larger work of the ALMAGAL project, has been to measure chemical abundances of different species and with a first application of seeing if the data can help constrain the gradient of various isotopic ratios with Galactocentric radius. Such gradients are expected in models of galactic chemical evolution. However, the study is more general in that it concerns the measurement of abudnances of species that ultimately can be used as astrochemical tracers of the star formation process in different environments.

Concerning the abundance ratio between the main stable isotopologue and other rarer isotopologues of a given molecular species, it is thought that this could be affected by local chemical processes, i.e., fractionation (e.g., Colzi et al., 2020). So such processes need to be understood in this context. On the Galactic scale, the absolute isotope value and its gradient is set by stellar nucleosynthesis, and the adoption of a specific galaxy formation and evolution model, such as the inside-out two infalls Galaxy formation model (Chiappini et al., 1997; Matteucci, 2021). For the ratio of ^{12}C to ^{13}C in particular, which are the main subject of our study, a positive gradient with increasing Galactic radial distance is expected and indeed observed by various studies. Some models predict a flattening at larger radii depending on the yields of massive stars and novae (e.g., Romano et al., 2019; Romano, 2022). However, the local chemical evolutionary process of selective-photo-dissociation may have an impact on the chemical conditions.

CHAPTER 2

Physical Processes in Massive Star and Star Cluster Formation

Massive star and star cluster formation require gravitational collapse, but this may also be regulated by the processes of magnetic field support, turbulence and feedback from the forming star or surrounding stars. However, the relative importance of these processes is unknown. In this chapter, we present a brief overview of these processes that are expected to play roles in controlling massive star and star cluster formation.

Gravity

Gravity is the ultimate force that drives the collapse of the molecular clouds to prestellar cores and then protostars. The Jean analysis determines the minimum length scale and mass in which the region of interest is dominated by gravity. The minimum length scale that is gravitationally unstable is known as the Jean length,

$$\lambda_J = \left(\frac{\pi c_s^2}{G\rho}\right)^{1/2}, \tag{2.1}$$

where $c_s = (\gamma kT/[\mu m_{\rm H}])^{1/2}$ is the sound speed and ρ is the density of the medium. The corresponding minimum mass that becomes gravitationally unstable is known as the Jean mass,

$$M_{\rm J} = \frac{4\pi}{3}\rho R^3, \tag{2.2}$$

where ρ is the density of the medium, and R is the radius equivalent to half of the Jeans length.

For an uniform density spherical system that is gravitationally bound and unstable and in the limit of negligible internal pressure support, the timescale for collapse is described as the "free-fall" time and is given by:

$$t_{\rm ff} = \sqrt{\frac{3\pi}{32G\rho}} = \frac{4.4\times10^4 \text{ yr}}{\sqrt{n_{\rm H}/10^6 \text{ cm}^{-3}}}, \tag{2.3}$$

where $n_{\rm H}$ is the number density of hydrogen nuclei, and the normalization to total mass density, ρ, assumes $n_{\rm He} = 0.1 n_{\rm H}$.

Magnetic fields

Magnetic fields act as an additional pressure term that can provide support against gravitational collapse. The classical method to estimate the field strength via the Davis-Chandrasekar-Fermi (DCF) method assumes flux freezing and equipartition in the turbulence and magnetic energy. Assuming that the dispersion in the magnetic field direction is due to turbulent motions, which are characterized by a 1D velocity dispersion σ_v, and the dispersion of field direction about some local mean value is represented by the dispersion of polarization angles, σ_θ, i.e., assuming dust grains align with their major axes perpendicular to field direction, then the plane of sky magnetic field strength can be evaluated by the following equation:

$$B_0 = Q\sqrt{4\pi\rho}\frac{\sigma_v}{\sigma_\theta}, \tag{2.4}$$

where Q is a factor related to the geometry (usually set equal to 0.5, e.g., Heitsch et al., 2001; Padoan et al., 2001; Ostriker et al., 2001).

However, the assumption and the equation of DCF have recently been under extensive review (see, e.g., Liu et al., 2022, for a review). Different modifi-

cations of DCF methods have been proposed. In particular Skalidis & Tassis (2021) proposed an alternative expression, derived from the assumption of compressible turbulence, i.e.,

$$B_0 = \sqrt{2\pi\rho}\frac{\sigma_v}{\sqrt{\sigma_\theta}}. \tag{2.5}$$

This method of estimation is thought to be more accurate in the trans-Alfvénic regime, where it predicts field strengths that can be significantly smaller than the classical DCF method. It should be noted that both of these DCF-type methods ignore the effects of gravity in distorting B-field orientations.

The relative importance of the magnetic energy and gravitational energy in a structure is described by the mass-to-flux ratio, λ. The critical mass-to-flux ratio for gas to be able to collapse against magnetic pressure is defined by (e.g., Mouschovias & Spitzer, 1976; Nakano & Nakamura, 1978):

$$\lambda_{\rm crit} = \left(\frac{M}{\Phi}\right)_{\rm crit} = \frac{c_\Phi}{G^{1/2}}, \tag{2.6}$$

where Φ is the magnetic flux and $c_\Phi = (2\pi)^{-1}$ is the magnetic critical mass coefficient, a dimensionless coefficient related to the cloud's shape and magnetic flux distribution (Nakano & Nakamura, 1978; Myers & Basu, 2021). The equation that computes the corresponding mass-to-flux ratio maps in units of the critical value is presented below

$$\lambda_\Phi = \frac{(M/\Phi)}{(M/\Phi)_{\rm crit}} = 2\pi\sqrt{G}\left(\frac{\Sigma}{B}\right). \tag{2.7}$$

The mass-to-flux ratio provides information on the relative importance of the magnetic field compared to gravity. If $\lambda_\Phi > 1$, the cloud will collapse because magnetic fields are not able to support against gravity, while $\lambda_\Phi < 1$ indicates magnetic fields are sufficient to support against gravitational collapse. If $\lambda > \lambda_{\rm crit}$, the system is said to be magnetically supercritical, i.e., $B-$fields cannot prevent collapse. If $\lambda < \lambda_{\rm crit}$, the system is said to be magnetically subcritical, i.e., $B-$fields prevent collapse, but only in directions perpendicular to the field lines and only if the material is well-coupled to the field lines by being sufficiently ionized.

Molecular clouds are mostly neutral. Only the ions are directly coupled

to the magnetic fields and neutral species can undergo "ambipolar" drift across field lines (e.g., Ward-Thompson & Whitworth, 2011). For a structure with length scale L and threaded by magnetic field with an average uniform strength B, the ambipolar diffusion timescale, $t_{\rm AD}$, is:

$$t_{\rm AD} \sim \frac{8\pi L^2}{B^2} n_n n_i \langle \sigma v \rangle \frac{\mu_n \mu_i}{\mu_n + \mu_i}, \tag{2.8}$$

where n_n, n_i are the number density of neutral and ionic species, respectively, μ_n and μ_i are the mean masses of these neutral and ionic species, and $\langle \sigma v \rangle$ is the collisional rate coefficient between the ionic and neutral species. For typical conditions, $t_{\rm AD}$ can be about 10 times longer than $t_{\rm ff}$.

Turbulence

The large-scale gas motions in molecular clouds are observed to be supersonically turbulent (e.g., Krumholz, 2011). Statistical properties of the turbulence may depend on the environmental and star formation properties of the cloud (see, e.g., Burkhart, 2021, for a review). Two basic parameters that are used to describe the observed properties of turbulent gas are the Reynolds number and the sonic Mach number. The Reynolds number is defined by the following equation at a length scale (L), gas velocity (v) and viscosity (ν):

$$\mathrm{Re} = vL/\nu. \tag{2.9}$$

Gas flow with a low Reynolds number is characterized by ordered, laminar flow. Gas flow with a large Reynolds number develops turbulence.

The sonic Mach number (M_s) is the ratio of turbulent velocity dispersion to sound speed. In molecular clouds, the temperatures are $\sim 10\,\mathrm{K}$, i.e., with sound speeds of $\sim 0.2\,\mathrm{km\,s^{-1}}$. Observed 1D velocity dispersions of IRDCs and GMCs can be ~ 1 to 10 $\mathrm{km\,}s^{-1}$, implying $M_s \sim 5$ to 50. Thus the turbulence is described as being supersonic, which is expected to lead to a network of shock-compressed regions. Shocks dissipate energy, so supersonic turbulence is expected to decay relatively quickly, i.e., with an exponential decay time that is about equal to a flow crossing time $t_{\rm cross} = L/v$, which is similar to a free-fall time for a self-gravitating cloud.

The classic study by Larson (Larson, 1981) found that the internal velocity dispersion of CO velocity spectra (Δv) is correlated with the cloud size (L).

The correlation can be described by a power-law ($\Delta v \propto L^{0.38}$). More recent studies find a power law index of about 0.5 McKee & Ostriker (see, e.g., 2007). The value of this index, i.e., describing a "line width - size relation", is an important property to describe the nature of interstellar turbulence.

An important property of turbulent gas flow in relation to magnetic fields is the potential anisotropic nature of the flow. If the magnetic field is dynamically important, then a greater degree of anisotropy is expected, with energy dissipation perpendicular to the $B-$field happening faster than along the field, i.e., motions are more constrained in directions perpendicular to the $B-$field. This aspect is summarized in Figure 2.1. The turbulence eddies are represented as ellipses, that have major axes in a direction aligned with the local magnetic field direction, while the minor axis is orthogonal to this. Thus spatial gradients in velocity are expected to be largest in directions perpendicular to the $B-$field. This opens up the possibility of kinematic methods for inferring magnetic field orientation (see, e.g., Burkhart, 2021, for a review).

Virial theorem: dissecting the relative importance of magnetic fields, turbulent, and gravity

The virial theorem provides the mathematical framework to analyze the effects of self-gravity, turbulence and magnetic fields in molecular clouds (Bertoldi & McKee, 1992). A cloud in virial equilibrium599 satisfies the following condition

$$0 = 2E_{\rm K} + E_{\rm B} + E_{\rm G}, \tag{2.10}$$

where $E_{\rm K}$, $E_{\rm B}$, and $E_{\rm G}$ are, respectively, the total kinetic energy, magnetic energy, and the gravitational potential energy. Following Bertoldi & McKee (1992), the gravitational energy of an ellipsoidal cloud is given by

$$E_{\rm G} = -\frac{3}{5} a_1 a_2 \frac{GM^2}{R}, \tag{2.11}$$

where G is the gravitational constant, M is the mass of the cloud, and R is the radius of the cloud. Here $R = \sqrt{ZR}$ is the geometric mean of the semi-major (Z) and semi-minor (R) axes of the cloud. Finally, a_1 and a_2 are parameters that describe the effects of the internal density distribution and the cloud ellipticity, respectively.

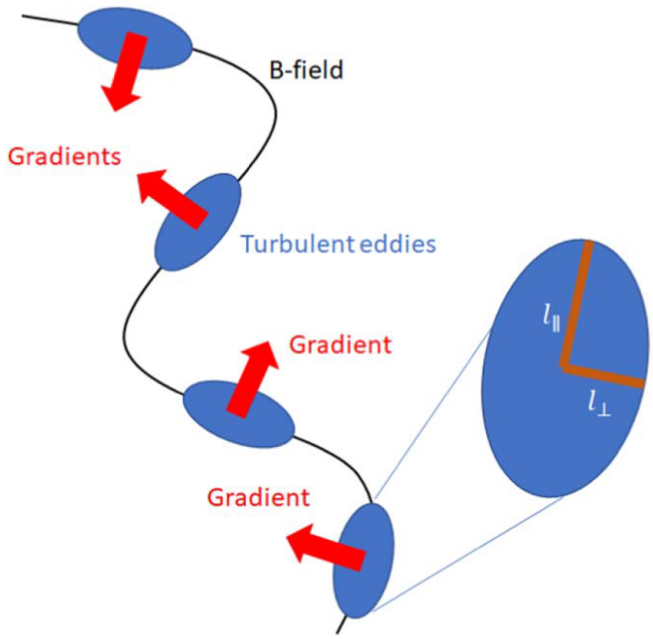

Figure 2.1: Schematic diagram adopted from Lazarian et al. (2018) showing turbulent eddies under the influence of a dynamically important magnetic field. The elongations of the turbulent eddies are aligned with the magnetic field direction. Notice that the anisotropy is related to the local magnetic field direction.

The kinetic energy takes the following form

$$E_{\rm K} \equiv \frac{3}{2}(\rho\sigma_v^2 - \rho_0\sigma_{v_0}^2)V_{\rm cl}, \tag{2.12}$$

where σ_v is the total 1-D velocity dispersion, ρ is the averaged density of the structure of consideration. Here we also include the surface term, which is based on the ambient medium's 1-D velocity dispersion, $\Delta_{v_{0,tot}}$, and density, ρ_0. Here $V_{\rm cl}$ is the volume of the structure, i.e., defined by $V_{\rm cl} = \frac{4}{3}\pi y R^3$ where y is the aspect ratio between the major and minor axes as defined above. Finally, the magnetic energy is

$$E_{\rm B} = \frac{1}{8\pi}\left(B^2 - B_0^2\right)V_{\rm cl}, \tag{2.13}$$

where B is the magnetic field in the cloud. Here, we include the surface term measured by taking the ambient magnetic fields, which are normally measured in the ambient medium surrounding the structure of consideration.

The metric that characterizes the relative importance of each term is via the virial parameter. The kinetic viral parameter defines the ratio between the kinetic energy and gravitational energy

$$\alpha_{\rm K} \equiv 2a\frac{E_K}{|E_G|}. \tag{2.14}$$

The ratio between the gravitational and magnetic energy is revealed by the mass-to-flux ratio described above. The total energy form of the viral parameter combining kinetic and magnetic energies is as follows Bertoldi & McKee (1992) and Liu et al. (2020)

$$\alpha_{\rm K+B} \equiv \sqrt{\left(\alpha_{\rm B}^2 + \frac{\alpha_{\rm vir}^2}{4}\right)} + \frac{\alpha_{\rm vir}}{2}. \tag{2.15}$$

By evaluating the dynamical status of IRDCs and the cores with the virial parameters and the Alfvenic Mach numbers across different regions of the IRDCs and the cores, it will be possible to characterize the dominant forces in action in massive star and star cluster formation. The maximum mass supported by thermal pressure alone for an unmagnetized cloud is defined by

the Bonnor–Ebert mass

$$M_{\rm BE} = 1.182 \frac{\sigma_{\rm th}^3}{\left(G\rho_0\right)^{1/2}} \tag{2.16}$$

In a similar manner, the maximum mass that can be supported from magnetic fields alone is the magnetic critical mass, which takes the form as follows (Bertoldi & McKee, 1992; Tan et al., 2013)

$$M_{\rm c,B} = 1.62 \left(\frac{R_c}{Z_c}\right)^2 \left(\frac{B_{\rm c,crit}}{100\mu{\rm G}}\right)^3 \left(\frac{n_{\rm H,c}}{10^5\ {\rm cm}^{-3}}\right)^{-2} M_\odot. \tag{2.17}$$

Both supersonic turbulence and magnetic fields play regulating roles in massive star and star cluster formation. The square root of the ratio between kinetic and magnetic energy is equivalent to the square of the Alfven Mach number ($M_{\rm A}$).

$$\sqrt{\frac{E_K}{E_B}} = \frac{\sigma_v}{v_a} = M_{\rm A}, \tag{2.18}$$

where $\mathrm{v_a} = \frac{B}{\sqrt{4\pi\rho}}$. Measurements of the Alfven Mach number provide crucial information on the relative importance of magnetic fields and thus put constraints on massive star formation models.

CHAPTER 3

Observational methods

High-mass star-forming regions are deeply embedded within molecular clouds, which are opaque in the optical and infrared regimes. Hence, they are best studied at far-infrared (MIR, $> 3\mu m$) to radio (cm) wavelengths. Single-dish telescopes and interferometers are the main facilities to observe these high-mass star-forming regions. However, the atmospheric water precipitations can absorb the radiation and strongly limit observations, particularly in sub-mm to mm wavelengths. Hence, many ground-based radio telescopes are built at high altitudes and dry (low precipitate water vapour, PWV) Furthermore, water and oxygen bands in the troposphere of the Earth's atmosphere absorb incoming radiations, which motivates MIR and FIR air-borne and space-borne telescopes. This chapter summarizes key elements in the observational methods used to obtain data to study massive star and star cluster formation.

3.1 Single dish telescopes

In this thesis we have obtained and analyzed data from different single dish telescopes from ground based to space based. A gallery of selected single-dish telescopes is presented in Figure 3.1. In general these telescopes are built at

Figure 3.1: Gallery of single dish telescopes used to gather data for this thesis. Top left: The Atacama Pathfinder Experiment telescope (APEX) telescope (Credit: ESO). Top tight: The Green Bank Telescope (GBT) (Credit: GBT). Bottom left: Stratospheric Observatory for Infrared Astronomy (Credit: SOFIA). Bottom right: IRAM-30m telescope (credit: IRAM).

sites of high elevation ($>$ 3000 m) and dry locations where the precipitate water vapour level is low. However, the transparency of the atmosphere in the MIR and FIR bands is very low. Hence, airborne or space telescopes are required to make astronomical observation possible (e.g., SOFIA, Herschel). Furthermore, space-based telescopes often offer much higher sensitivity to faint emission given the lack of thermal emission from the atmosphere.

The ability for a given single-dish telescope to resolve a certain astronomical target depends on the diameter of the antenna, D, and the wavelength of the light, λ. From diffraction theory, the following equation gives the angular resolution (θ) in radians:

$$\theta = \frac{\lambda}{D}. \tag{3.1}$$

Hence, it is also noted that for a fixed antenna size, the resolution increases at

shorter wavelengths. The electromagnetic radiation the antenna receives by reflection at the primary dish is gathered to the focus before being detected by the receiver.

3.2 Interferometry

Interferometry (see gallery in Figure 3.2 of selected facilities) enables observations with high angular resolution that are important to study regions of massive star formation that are located at large distances. The resolution scale of an interferometer is determined by the ratio of the wavelength to the maximum length of the baseline ($D_{\rm array}$ via

$$\theta \approx \frac{\lambda}{D_{\rm array}}. \tag{3.2}$$

Taking G28.2-0.05 as an example, this massive protostellar system has a ring-like structure with a scale of $0.7''$ and is at a distance of 5.7 kpc. To have five sampling elements across the source thus requires an angular resolution of roughly $0.14''$. Interferometers such as the Atacama Large Millimeter/submillimeter Array and the Next Generation Very Large Array (ngVLA) are thus needed to probe the detail structure of these distance massive protostellar systems.

However, as a trade-off, the interferometer filters out the intensity of extended emissions, i.e., only features up to a certain largest scale will be recovered, also known as the maximum recoverable scale (MRS). The MRS is defined by the resolution of the shortest baseline in the configuration.

The basics of interferometry can be described by considering two antennas, as illustrated in Figure 3.3. The source emission will reach antennas A and B at different times due to the orientations of the array baseline (Figure 3.3). The geometric delay is described by the vector's dot product pointing toward the source $\vec{S}$, and the baseline vector $\vec{b}$ divides by the speed of light. Due to the Earth's rotation, the baseline vector's component will change and the changes of the vector could be defined in the displacement of the source ($\Delta\vec{S}$) from some reference fixed position ($\overrightarrow{S_0}$), described by the following equation

$$\vec{B}_{\parallel}\overrightarrow{S_0} + \vec{B}_{\perp}\Delta\vec{S} = \vec{B}_{\parallel}\overrightarrow{S_0} + ux + vy. \tag{3.3}$$

Figure 3.2: Gallery of interferometer arrays Top left: The Atacama Large Millimeter/submillimeter Array (ALMA) (Credit: ESO). Top tight: The Karl G. Jansky Very Large Array (VLA) (Credit: Bettymaya Foott, NRAO/AUI/NSF). Bottom : The Submillimeter Array (SMA) (Credit: ESO).

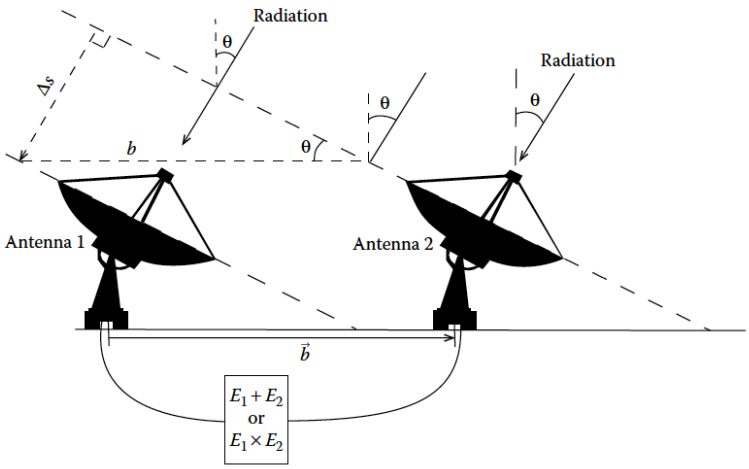

Figure 3.3: Figure adopted from Snell & Kurtz (2019). The two antennas are separated by a baseline distance b. As the radiation reaches antenna 2, a geometric delay, i.e., caused by the extra path length that the wave must travel to reach antenna 1, is Δs, which is the dot product of the unit vector pointing toward the source and the baseline vector b. Here θ is the angle between the direction normal to the baseline vector and the vector pointing toward the source

The corresponding coordinate system that traces the position of the vector $\vec{B}_\perp$ is known as the uv-plane. The uv distance is then defined by $\sqrt{(u^2+v^2)}$ in the unit of λ. The amplitude of that point in the uv space is called visibility, the Fourier transform of the source's intensity in real space via the Van Sitter-Zernike theorem. In practice with observations at different baselines, it requires combining the data to retrieve the desire uv coverage to image the intensity distribution of the source. Furthermore, as it is impossible to put two antennas at the same spot, the interferometric observation is normally limited by the zero spacing. This will led to "missing flux", in which the extended emissions at scale larger than the MRS will be filtered out. It is a normal practice to perform a flux recovery check between interferometric data and single dish to quantify the percentage of missing flux. Hence, single-dish telescope observations are an important complement to providing zero spacing in the uv space and recovering the missing flux from the interferometer due to an incomplete sampling of the uv space.

3.3 Measuring magnetic field morphology in massive star forming regions

One of the main ways to trace the plane of sky magnetic field morphology is via the polarized emission from either the background starlight or the thermal emission from dust grains. The mechanism of alignment of dust grains with magnetic field is crucial for these methods (see, e.g., Andersson et al. 2015 for a review). Here we provide a brief summary of radiative alignment torque (RAT) mechanism of grain alignment.

The (b-)RAT mechanism predicts that in the presence of an anisotropic radiation field, e.g., coming from an embedded protostar or an external UV source, dust grains are aligned with their major axes perpendicular to magnetic field lines. The radiation will create a torque causing a grain to spin. The rotational axis of the grain precesses around the magnetic field direction, while paramagnetic dissipation tends to align the grains with their long axes perpendicular to the magnetic field. This alignment is independent from the radiation direction or the magnetic field direction.

With the grains aligned with their long axes perpendicular to the local magnetic field direction, background star light is most likely to be attenuated via the selective dichroic extinction leading to polarized received stellar emission

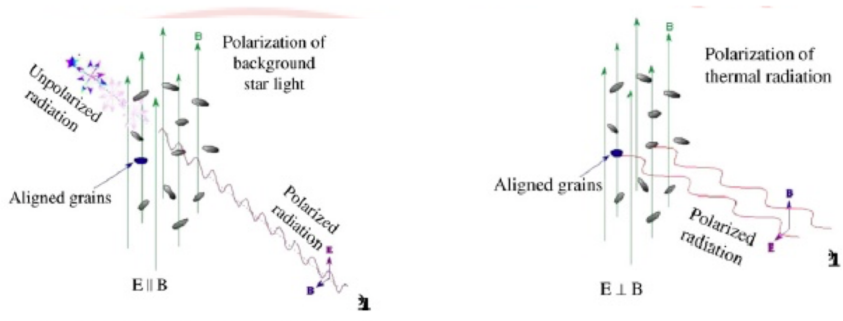

Figure 3.4: Schematic figures showing the two polarization mechanisms. Left: Polarization of background star due to selective extinction, which the polarization orientation is parallel to the magnetic field direction. Right: Polarization of the thermal dust emission, in which the polarization orientation is normal to the magnetic field direction.

with orientation align with the magnetic field direction. On the other hand, the thermal emission from magnetically aligned grains is more likely to have electric field vectors along the plane containing the long axis. Thus, the polarized dust emission orientation is perpendicular to the magnetic field direction. Figure 3.4 present schematic figures of these two polarization mechanisms.

The fundamental quantities of polarization are described by the Stokes parameters. Note, for describing linear polarization, requires the Stokes Q, U, and the total intensity I. The Stokes Q and U are defined as:

$$\begin{aligned} Q &= p\cos 2\theta \\ U &= p\sin 2\theta, \end{aligned} \tag{3.4}$$

where θ is the polarization position angle and the fraction of polarisation is

$$p = \frac{\sqrt{Q^2 + U^2}}{I}. \tag{3.5}$$

Then, the polarisation intensity is defined as

$$P = \sqrt{Q^2 + U^2}. \tag{3.6}$$

The corresponding polarization angle in degrees is defined by

$$\theta = \frac{1}{2}\frac{180}{\pi}\tan^{-1}\left(\frac{U}{Q}\right). \tag{3.7}$$

Note that the fraction of polarization is restricted to positive values, and with addition of small numbers in Q and U if the signal to noise is low, will result in a positively skewed Rice distribution (Rice, 1944). The correction applied is called 'debiasing', in which the debiased polarization fraction is equal to $p' = \sqrt{p^2 - \delta^2}$. In general a data cut is made on the signal to noise ratio (SNR) in Stokes I and/or in the polarization fraction. The sensitivity in polarisation fraction can be inferred from the SNR of Stokes I by

$$\sigma_p \sim \frac{\sqrt{2}}{(SNR)_I}. \tag{3.8}$$

For example, if we want to have a typical sensitivity of 2%, then we require a $SNR_I \sim 70$.

CHAPTER 4

Summary of included papers

4.1 Paper I

In the first paper, we present a detailed characterization of the physical properties of the massive protostellar system G28.2-0.05 (Figure 4.1). The study was motivated by the apparently isolated nature of the source as a means to more stringently test massive star formation theories. The data was based on ALMA Band 6 observations. The data was reduced by the pipeline and manual reduction was performed on the most extended configuration data. All imaging and self-calibrations were performed with CASA (ver. 5.6.1-8) (McMullin et al., 2007).

We first inspected the overall 1.3 mm continuum morphology and detected a ring-like structure at a scale of about 2,000 au. A similar structure has been seen by the VLA at 1.3 cm, suggesting it traces ionized gas, i.e., from a HC HII region. We characterized the radio SED, including with an in-band SED analysis, to estimate the contribution of dust emission to the 1.3 mm flux. The dust appears to be concentrated on one side of the ring at the main mm continuum peak, which we identify as the likely location of the massive protostar (see also below). The regions just beyond the ionized ring, also

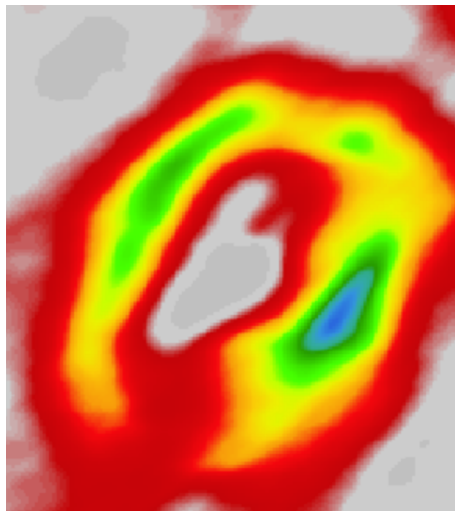

Figure 4.1: ALMA 1.3 mm total continuum image of the massive protostellar system G28.2-0.05.

appear to be dominated by dust emission.

We examined line emission in the ALMA data. The H30α recombination line also traces ionized gas. It shows a strong line of sight velocity gradient at the location of the main mm continuum peak, which is further evidence that this is the location of the massive protostar. A dynamical mass estimate is made of the source from these data. Several hot core molecular species are also identified, with emission in the vicinity of the mm continuum peak. However, a more extensive study of the astrochemistry of the source is presented in Gorai et al. (2023). Finally, high velocity CO(2-1) emission was detected tracing a wide-angle bipolar outflow that is driven from the region and extends to large scales.

4.2 Paper II

Magnetic fields may play a crucial role in setting the initial conditions of massive star and star cluster formation. To investigate this, we report SOFIA-HAWC+ 214 μm observations of polarized thermal dust emission and high-resolution GBT-Argus $C^{18}O$(1-0) observations toward the massive Infrared Dark Cloud (IRDC) G28.37+0.07. Considering the local dispersion of B-field orientations, we produce a map of B-field strength of the IRDC, which exhibits values between $\sim 0.03-1\,\mathrm{mG}$ based on a refined Davis–Chandrasekhar–Fermi (r-DCF) method proposed by Skalidis & Tassis. Comparing to a map of inferred density, the IRDC exhibits a $B-n$ relation with a power law index of 0.51 ± 0.02, which is consistent with a scenario of magnetic field-regulated anisotropic collapse. Consideration of the mass-to-flux ratio map indicates that magnetic fields are dynamically important in many regions of the IRDC. A virial analysis of a sample of massive, dense cores in the IRDC, including evaluation of magnetic and kinetic internal and surface terms, indicates consistency with virial equilibrium, sub-Alfvénic conditions and a dominant role for $B-$fields in regulating collapse. A clear alignment of magnetic field morphology with direction of steepest column density gradient is also detected. However, there is no preferred orientation of protostellar outflow directions with the $B-$field. Overall, these results indicate that magnetic fields play a crucial role in regulating massive star and star cluster formation and so need to be accounted for in theoretical models.

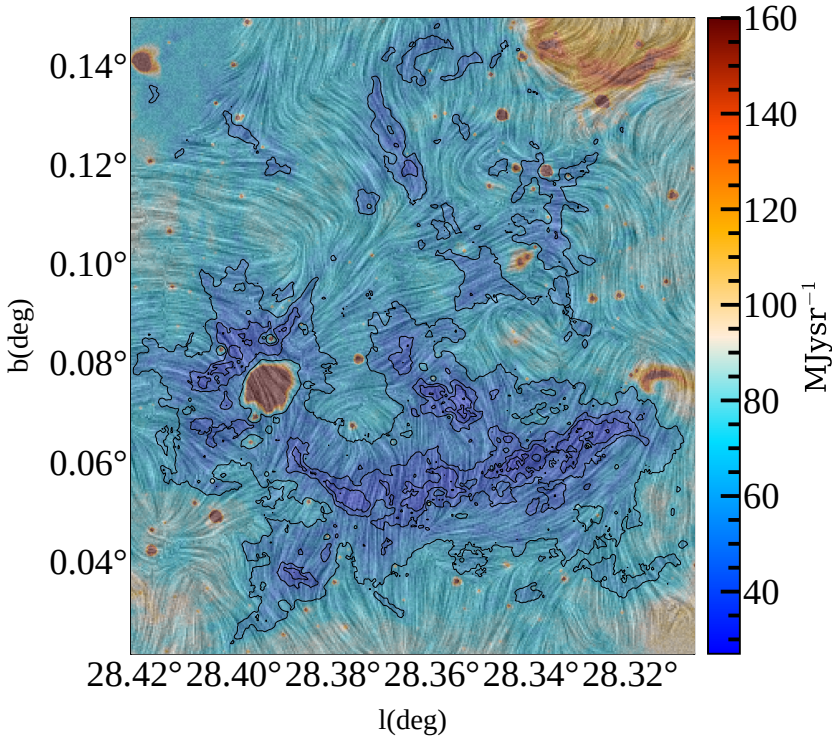

Figure 4.2: 8μm intensity map of G28.37+0.07 with the inferred plane of sky magnetic field component overlaid as a "drapery" pattern.

4.3 Paper III

The isotopic ratios of carbon, nitrogen, and sulphur in high-mass star-forming regions across Galactic radial distances provide a crucial perspective for constraining stellar evolution and nucleosynthesis of both supernovae (SNe) and asymptotic giant branch (AGB) stars. Furthermore, the Galactic radial distribution of isotopic ratios also strongly constrains the chemical initial conditions of star and planet-forming regions. We examined the main carbon isotope ratio of ^{12}C to ^{13}C using a large sample of massive star-forming regions from the ALMAGAL survey(Figure 4.3). The ALMAGAL survey is an ALMA large program that systematically sampled a large number of high-mass clumps with mass $> 500\ M_{\odot}$ at a resolution of 3000 au assuming an average distancesfrom the Sun of 3 kpc. We apply standard techniques extensively used in spectral studies to attempt to determine the carbon isotopic ratio as a function of Galactocentric distance using H_2CO(3-2) and HC_3N(24-23) and their ^{13}C isotopologues. We find, in contrast to many previous studies, a lack of a radial gradient, which hints that local chemical processes may already be shaping the chemical evolution of stars and planet formation regions at $\sim$0.1 pc scales. However, we also demonstrate that optical depth plays a crucial role in potentially biasing systematically our (and other studies) of the carbon isotope ratio, making the interpretation difficult. We further quantify the effect of optical depth with single-dish data. Our results show that achieving high accuracy of the isotopic ratio measurement requires a multi-line analysis.

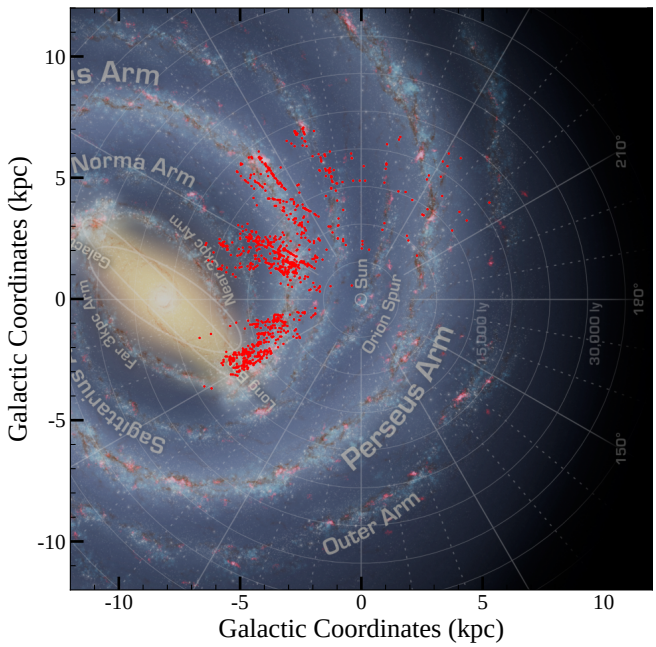

Figure 4.3: Spatial distribution of all ALMAGAL clumps (red dots) overlaid on a top-down view of the Milky Way.

4.4 On-going projects and other selected papers

Turbulence and magnetic fields in IRDC G38.9-0.74

Introduction

The roles and relative importance of self-gravity, turbulence, magnetic fields and feedback in massive star and star cluster formation remain uncertain (e.g., Tan et al., 2014; Rosen et al., 2020). In particular, it is challenging to measure the properties of magnetic fields (see §2), with most practical methods of inferring $B-$field morphology and strength in star-forming molecular clouds relying on indirect methods, especially via mapping of polarized emission that is assumed to arise from the alignment of nonspherical dust grains with magnetic field directions (e.g., Li et al., 2014). Significant advances in this kind of observational data have occurred recently with the results of PLANCK, BLAST-POL, JCMT-POL2, and SOFIA-HAWC+. Another relatively novel method is to try and infer the effect of magnetic fields on turbulent motions (see §1). Such methods have typically been calibrated against idealized simulations of turbulence, but there have been relatively few studies that test their results against independent observational measures of $B-$fields, such as from polarizaration. This comparison is the primary goal of this project, with the target to be studied an example Infrared Dark Cloud (IRDC) that has been observed with high spatial and kinematic resolution in CO lines and has had its polarization morphology mapped in the FIR.

IRDCs were identified via their high opacity at mid infrared (MIR) wavelengths (e.g., Rathborne et al., 2006; Barnes et al., 2021). These massive dense clouds are known to be the progenitors of massive stars and star clusters (e.g., Butler & Tan, 2012; Kainulainen & Tan, 2013; Hernandez & Tan, 2015; Sokolov et al., 2017). Direct observations of the magnetic field strengths in IRDCs are very challenging, e.g., because molecules normally used for Zeeman measurements, like CN, are frozen out onto dust grains. Some constraints on $B-$field morphology and strength have been derived based on maps of polarized dust emission and by utilizing the Chandrasekhar & Fermi method (Chandrasekhar & Fermi, 1953). For example, Pillai et al. (2015) and Soam et al. (2019) have found relatively ordered degrees of polarization and inferred that dynamically important magnetic fields are presented in IRDCs. However, there are significant uncertainties with this method of $B-$field estimation, including its reliance on the uncertain physics of dust grain alignment with

$B-$fields. Alternative methods are thus needed to compliment as well as to provide independent information on the magnetic field properties.

Models and simulations of interstellar turbulence (e.g., Goldreich & Sridhar, 1995) allow predictions to be made for the influence of magnetic fields on velocity anisotropies and how these may be inferred from analysis of spectral lines cubes of molecular lines, especially CO. have made ways to various techniques to infer magnetic field orientations and other properties using the spectral line cube of molecular lines (see, e.g., Burkhart, 2021, for a review). In particular, the Velocity Channel Gradient (VCG) technique has been shown to capable to reveal magnetic field morphology and other properties (e.g., Yuen & Lazarian, 2017; Lazarian et al., 2018).

Observationally, the VCG method has been applied to a few low-mass star-forming regions (e.g., Hu et al., 2019; Heyer et al., 2020) and in the massive star forming region DR21 (Alina et al., 2020). However, it is unclear how reliable VCG may be in regions with strong outflow feedback from star formation. Thus additional observational studies are needed to test VCG analysis, ideally in early-stage clouds, like IRDCs, that may be relatively free of feedback.

The IRDC G38.9-0.74 (kinematic distance of 2.7 kpc) is one (Cloud I) of the ten clouds (A-J) in the sample of Butler & Tan (2009), Butler & Tan (2012), and Kainulainen & Tan (2013), who produced high resolution MIR-based extinction maps of the regions. Hernandez & Tan (2015) studied the kinematics and dynamics of these clouds, including Cloud I, using the relatively low resolution (about $46''$) ^{13}CO(1-0) data of the Galactic Ring Survey (GRS) (Jackson et al. 2006). The study by Cosentino et al. (2020) detected a wide spread of SiO morphology over Cloud I, which indicates a potential shock interaction with the nearby HII regions N74 and N75. Two cores have been identified toward the cloud, in which one has found with signatures of molecular outflow and in-fall signature based on single dish SiO studies, while the second core is more quiescent. The existence of both kinds of environment provides an ideal test-bed to for the VCG techniques.

Here, using IRDC G38.9-0.74 (Cloud I) as a test case, we present preliminary results from a project to perform the first comprehensive study of the magnetic field morphologies and properties of IRDCs utilizing the high-resolution (about $6''$) $^{13}\mathrm{CO}(1-0)$ Green Bank Telescope (GBT)-Argus observations, complimented with SOFIA-HAWC+ dust continuum polarimetry data.

Methods

Velocity Channel Gradient (VCG)

The VCG method using spectral line cube data is described in detail by Yuen & Lazarian (e.g., 2017), Lazarian et al. (2018), and Heyer et al. (2020).

In brief, the method applies a simple Sobel kernel to compute the gradient in intensities of a given "thin" channel map.The condition of being "thin" is simply that the velocity range of the channel map be smaller than the velocity dispersion of the cloud. Then the direction and magnitude of the gradient in intensity, i.e., brightness temperature, T, are described by

$$\nabla T_k(x,y,v) = \left[\left(\frac{\partial T_k(x,y,v)}{\partial x} \right)^2 + \left(\frac{\partial T_k(x,y,v)}{\partial y} \right)^2 \right]^{1/2}, \tag{4.1}$$

$$\Psi_{G,k}(x,y,v) = \arctan \left[\frac{\partial T_k(x,y,v)}{\partial x} / \frac{\partial T_k(x,y,v)}{\partial y} \right]. \tag{4.2}$$

In practice, the original map is dissected into multiple blocks which the mean of gradient in each block is computed. Here we take the block size to be the same as the three beam resolutions, which correspond to $18''$ by $18''$. This size is also equivalent to the SOFIA beam resolution.

Results

CO Kinematics

The overall ^{13}CO(1-0) integrated intensity morphology is presented in Figure 4.4. It shows peak intensities of about 50 K km/s, concentrated in several main clumps that are surrounded by a more extended structure. We also inspect the velocity spectrum (Figure 4.5) to infer the systemic velocity of the cloud of 41.2 km s^{-1}. We notice that this velocity is consistent with the 41.6 km s^{-1} that was reported in Rathborne et al. (2006).

Polarized Dust Emission

Figure 4.6 presents the Stokes I maps toward the G38.9-0.74 region. The overlaid HAWC+ inferred magnetic field directions shows ordered magnetic field morphology around the cloud. We only select polarization vectors that have

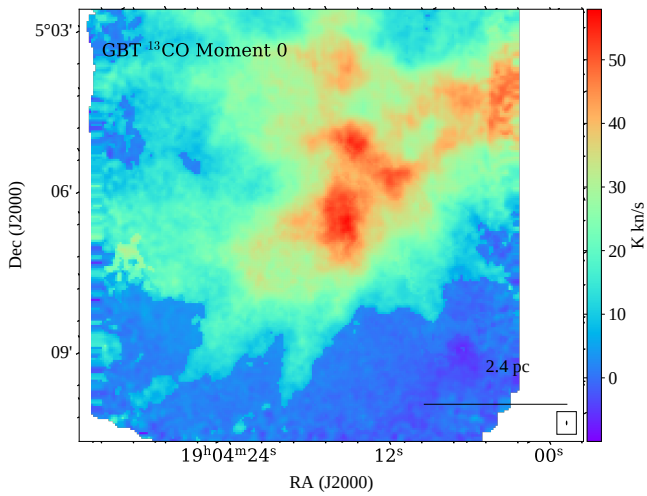

Figure 4.4: ^{13}CO(1-0) Moment 0 map of IRDC G38.9-0.74 integrated from $v_{\rm lsr}$ = 32 to 50 km s^{-1}.

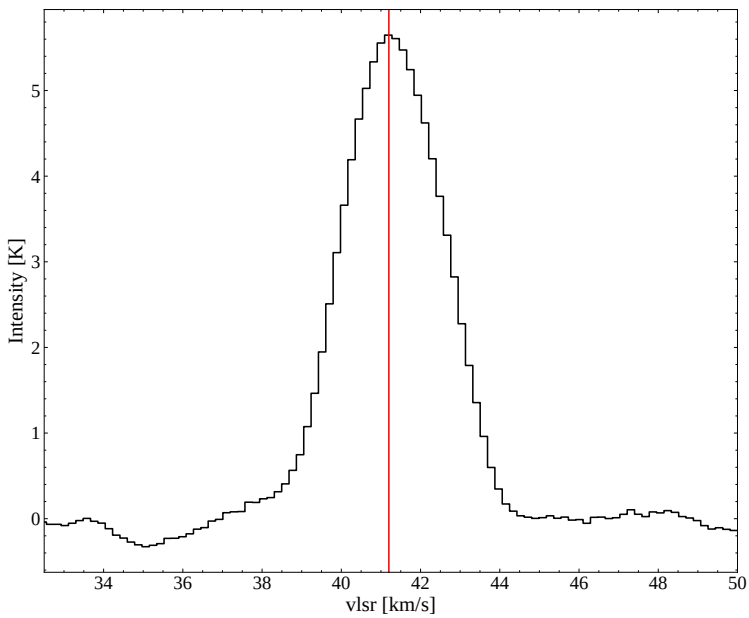

Figure 4.5: Averaged ^{13}CO(1-0) spectrum of G38.9-0.74. The red line shows the inferred systemic velocity of 41.2 km s^{-1}.

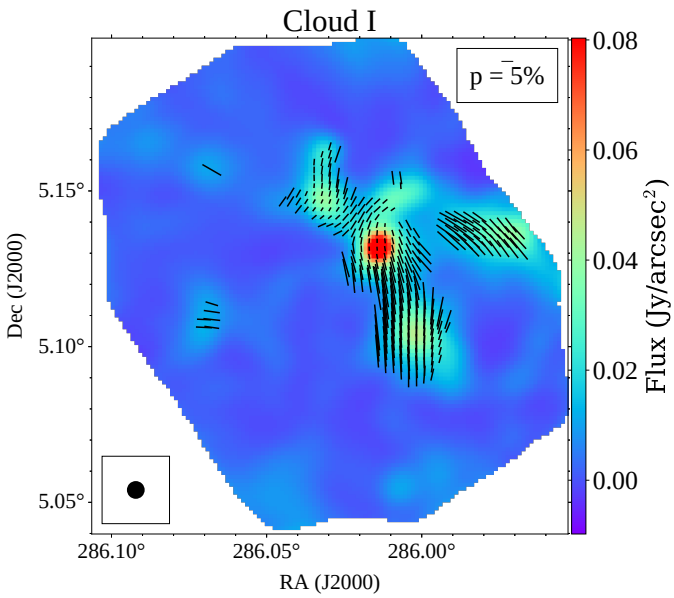

Figure 4.6: SOFIA 215μm Stokes I intensity map overlaid with the magnetic field direction.

$I/\sigma\ I \geq 50$, SNR(P)≥ 2, P(%)≤ 50, and the uncertainty of the polarization angle $\delta\theta <= 30$. However, we notice that most of the vectors seems to be off the main filament but detecting the nearby HII regions. None the less, as the GBT-ARGUS data cover the same region, thus allow us to compare the magnetic field morphology.

B-field Analysis

For the CO data, we carry out the VCG analysis on a thin channel near the peak of the spectrum. The results are shown in Figure 4.8. A first inspection of the overall morphology suggests no particular anisotropy in the direction.

Next, we show the HAWC+ inferred B-field orientations overlaid on the CO map of the IRDC. The map shows the presence of ordered polarization vectors detected toward the relatively bright regions, with much of the inferred B-field

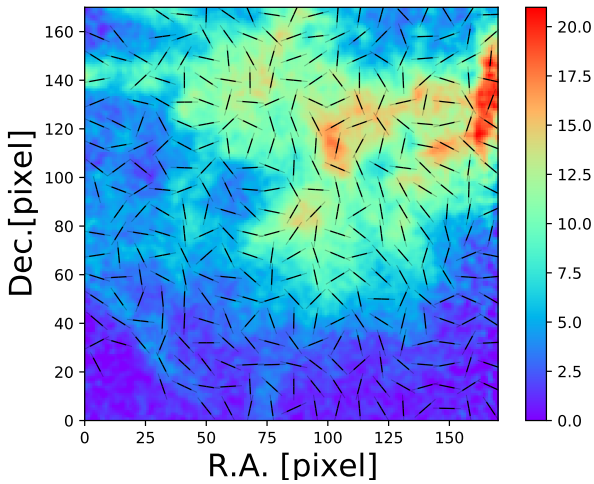

Figure 4.7: Top: ^{13}CO(1-0) Moment 0 map of IRDC G38.9-0.74 overlaid with the the HAWC+ 215μm Stoke I intensity contours (silver) and the 8μm intensity contours (black). The inferred magnetic field (by rotating the polarization angle with 90 degrees) is overlaid as vectors. The SOFIA beam size is presented in the bottom left corner with FWHM of 18$''$. We only select polarization vectors that have $I/\sigma\ I \geq 50$, SNR(P)$\geq$ 2, P(%)$\leq$ 50, and the uncertainty of the polarization angle $\delta\theta$ <= 30. Bottom: plane of sky magnetic field morphology inferred from the 13CO(1-0) spectral cube using the velocity gradient technique. The background presents the moment 0 map toward the velocity channel at the systemic velocity (peak of the spectrum).

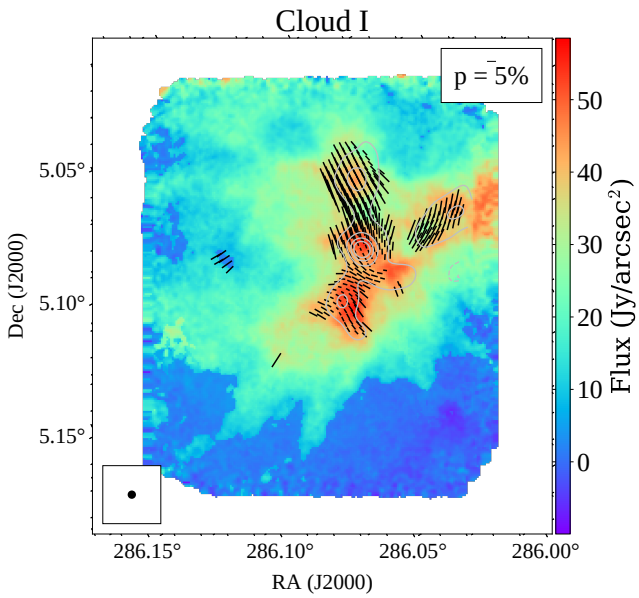

Figure 4.8: ^{13}CO(1-0) Moment 0 map of IRDC G38.9-0.74 overlaid with the the HAWC+ 215μm Stoke I intensity contours (silver) and the 8μm intensity contours (black). The inferred magnetic field (by rotating the polarization angle with 90 degrees) is overlaid as vectors. The SOFIA beam size is presented in the bottom left corner with FWHM of 18″. We only select polarization vectors that have $I/\sigma\ I \geq 50$, SNR(P)≥ 2, P(%)≤ 50, and the uncertainty of the polarization angle $\delta\theta \leq 30$.

vectors in the North to South direction.

Thus, from a preliminary analysis of these data, we do not see clear evidence of agreement between the VCG and dust polarization methods for inferring B-field orientation. Further work (Law et al. 2024, in-prep) is needed to examine the robustness of this conclusion adequately.

SOFIA-HAWC+ multi-wavelengths polarimetry of G28.2-0.05

Introduction

Magnetic field is ubiquitous in the interstellar medium and may play an crucial role in regulating (massive) the formation (e.g. see reviews by Li et al., 2014; Tan et al., 2014). However, measuring magnetic field is challenging as they are invisible, thus indirect methods are required to map and characterise the magnetic field properties. Polarized emissions from aligned dust grains are the main channel to probe and study the plane of sky component of the magnetic field orientations and corresponding aligned grain properties such as the sizes distributions and compositions. The two main polarization mechanisms of aligned grains are dichroic extinction and thermal dust re-emission (see Chapter 3.3). At a specific wavelength, the degree of contribution of each of the polarization mechanism is expected to relate to the dust opacity, particularly relate to the volume density of dust along the line of sights length (Reissl et al., 2014; Reissl et al., 2017). Synthetic multi-wavelengths polarisation observations suggested such a transition is expected to be seen at wavelengths $< 200\mu m$(Kuffmeier et al., 2020). At smaller scale close the the disk, the increase in optical depth would led to transition from emission to dichroic extinction from sub-millimeter and radio regime and have been proposed to explain a 90 degrees flip in polarisation orientations between millimeter ALMA and centimeter VLA observations (e.g. Guo et al. 2023). However, such flip has not been observed at the large scale, despite the availability of multi-wavelengths polarimetric data in range of $53\,\mu m$ to $870\,\mu m$. Possible reasons are that many of these regions contains star clusters and multiple sources, in which complicate the field morphology and thus not able to clearly identify such change. Hence, multi-wavelengths studies of relative isolated strong sources would be prime target to detect such transition (but also see (Kuffmeier et al., 2020)).

Recently, High-resolution ALMA data study showed that G28.2-0.05 hosts a massive protostar forming in a relatively isolated environment and a SED analyses predict a proto-stellar mass of about 40 $M_{\odot}$(Law et al., 2022). Such an isolated star formation environment provides a unique laboratory to study the dust polarization properties without complicated geometry or contamination due to clustering environment.

Methods

We carried out G28.20-0.05 has been observed at 53 μm and 214 μm by High-resolution Airborne Wideband Camera Plus (HAWC+) at the Stratospheric Observatory for Infrared Astronomy (SOFIA; Dowell et al. 2010; Harper et al. 2018). The SOFIA/HAWC+ 53 μm (Band A) and 214 μm (Band E) observations of G28.2-0.05 were carried out on the 7th of September 2021 as part of the SOFIA Cycle 9 observations (Proposal ID: 09_0164). Bands A and E provide an angular resolution of 4.85″ and 18.2″ full width at half maximum (FWHM), respectively. The observations were performed using the Nod-Match chop mode with a Lissajous scan pattern. The raw data were processed by the HAWC+ instrument team using the data reduction pipeline version 3.0.0. This pipeline includes different data processing steps, such as corrections for dead pixels and the intrinsic polarization of the instrument and telescope (Santos et al., 2019). The final 'Level 4' (science quality) data contains FITS images of the total intensity (Stokes I), debiased polarization degree p ($p' = \sqrt{p^2 - \sigma_p^2}$), polarization angle ($\theta_{pol}$), Stokes Q and Stokes U, and the corresponding uncertainties. The angular resolutions at the two wavelengths are 5.″45 and 18.″2, respectively. The resolution resolves scale greater than 10,000 au, thus we are probing the large scale polarization properties. The science ready data were delivered after pipeline reductions performed by the SOFIA science staff.

Results

Figure 1 summarise the dust polarizations orientations of G28.20-0.05 at 214 μm and & 53 μm (black & white vectors). When overlaying them together in the bottom panel, we see a 'flip' toward the source, the shorter wavelengths (white) polarization orientations run in the northwest to southeast direction. In contrast, the longer wavelength (black) polarization vectors exhibit a more complicated orientation, but the polarized vectors toward the source run in the northeast direction toward the southeast direction. To further quantify the 'flip', we plot in Figure 2 presents a histogram distribution of the polarization angle at (53 μm & 214 μm) respectively toward the primary source taken with an aperture size of 30″. The figure reveals a bimodal distribution, with the peak positions separated by about 85 degrees and a median of about 61 ± 18 degrees. Therefore, we identify a significant flip in polarization angle

orientations from 53 μm to 214 μm. The finding seems to be consistent with the prediction from simulation study (Kuffmeier et al., 2020). Hence, we emphasize the importance of multi-wavelengths polarimetry, and in particularly at wavelengths between 50 μm to 214 μm. Furthermore, proper and correct dust modelling and physics is required to characterise the interpret the dust polarization observations results. Multi-wavelengths from 50 μm to 870 μm dust polarization studies of more other relatively isolated massive protostellar objects (e.g. Lu et al., 2022; Fedriani et al., 2023) would further confirm this phenomena.

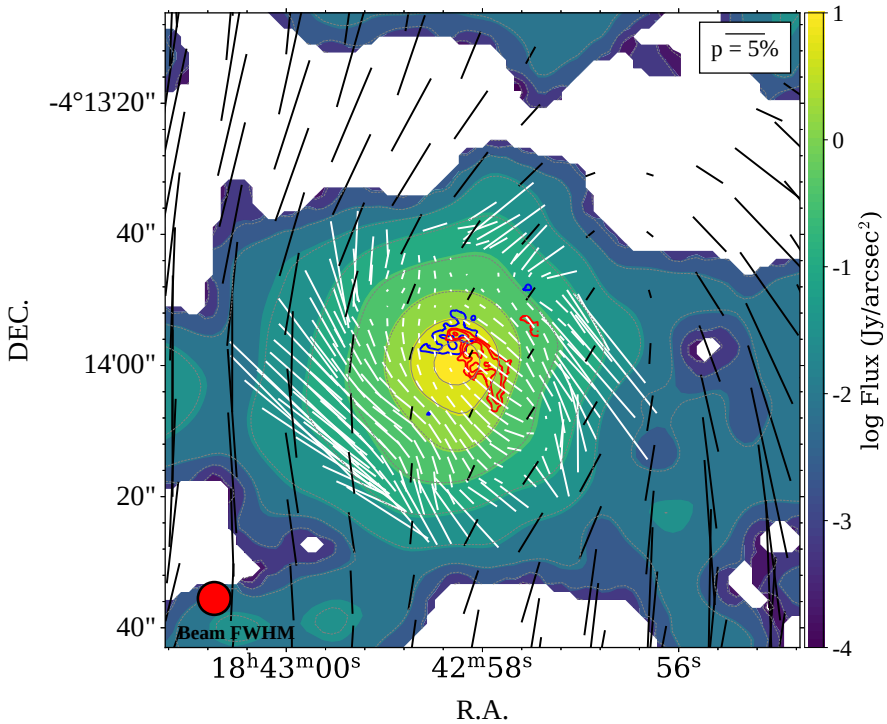

Figure 4.9: Summary of polarization data of G28.20-0.05 with HAWC+ 53 μm and 214 μm polarization vectors overlaid on the 53μm stokes I image. Black and white vectors respectively represent 214μm and 53μm polarization vectors with $SNR_I \geq 20$. The lengths of the vectors are scaled with the degree of polarization. The beam FWHM of SOFIA-HAWC+ at 53μm is presented in the bottom left. We notice a clear flip in the polarization orientation between 214μm and 53μm polarization vectors and become clearer toward the source centre.

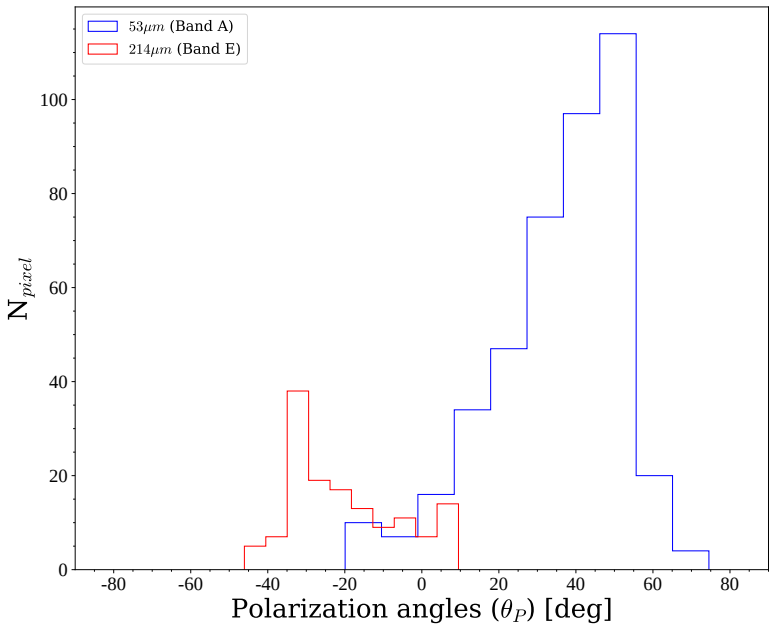

Figure 4.10: Histogram of polarization vectors within the central 0.5′ radius from the source center. A bi-modal distribution is observed with the a peak separation of about 85 deg.

Other selected papers with major contributions

As mentioned in the introduction, understanding the properties of interstellar turbulence in the presence of strong magnetic fields may provide a novel window to probe magnetic field properties and the effects of other physical processes (e.g., gravity, outflows, shocks). Various approaches to studying B-fields based on theories of interstellar magnetohydrodynamic (MHD) turbulence and turbulent reconnection have also been developed. Among them, one of the methods is the velocity gradient technique (a.k.a. thin channel intensity gradient), which has been applied extensively and claimed to trace magnetic field direction relatively consistently. However, most of these studies only compare to low-resolution ($5'$) PLANCK observations. Furthermore, there have been studies showing that outflow and gravity will significantly degrade the goodness of alignment (quantified by the metric called alignment measure) between the velocity gradient and the field direction. Here we calibrate the VGT with high resolution GBT ^{13}CO(1-0) and C^{18}O(1-0) toward IRDC G28.37+0.07. (Xu et al., 2023) applied a deep learning method CASI-3D (convolutional approach to structure identification-3D) to predict the orientation of magnetic fields. With the PLANCK dust inferred magnetic fields orientations as reference, the machine learning inferred field directions map is compared to the magnetic field orientation inferred from VGT and found to have a significantly better performance.

CHAPTER 5

Concluding Remarks and Future Work

Studying more massive protostars in a greater range of environments will allow further constraints on massive star formation theories. In particular, a more general survey of protostellar crowding around massive protostars, following our work on G28.2-0.05, is needed. The SOFIA Massive (SOMA) Star Formation survey, which has observed a large sample (> 50) massive protostars in different environments and evolutionary stages provides a prime database for follow-up studies with ALMA to carry out such analysis. In addition, the ALMAGAL survey, which has surveyed more than 1000 massive clumps, also serves as a rich database to search for relatively isolated massive clumps and follow up with high-resolution ALMA observations to characterise the physical and protostellar properties. Furthermore, the SOMA-POL survey with JCMT-SCUPOL, which so far has sampled about 15 massive star forming regions from the main SOMA sample, will provide a valuable dataset to characterise the magnetic field properties and dissect the role of magnetic fields in massive star and star cluster formation.

Analysis of the remaining IRDCs in the POLIMAP survey will further explore the environmental factors that regulate massive star and star cluster formation. In particularly, combining other single dish and interferometric

data, most of these clouds will able to probe the turbulent statistics from cloud ($>$ 10000 AU) to disk ($<$ 1000 AU) scales. This will provide insights on the role of turbulence and magnetic fields in a wide range of scales of massive star and cluster formation(Law et al. 2024 in-prep, see Chapter 6). Multi-wavelengths polarimetry is essential to study aligned dust properties and dominant polarization mechanisms as a function of wavelengths. To this end, multi-wavelength polarimetry data of G28.20-0.05 provide a unique 'test-bed' (Palaro,Law,C.Y. et al. 2024, in-prep, Law et al. 2024, in-prep).

Finally, as established in Paper III, multi-transition molecular line analysis is timely to correctly measure the isotopic ratio of carbon, nitrogen, and sulphur and compare with the Galactic radial gradient of the isotopologue ratio to test predictions of Galactic chemical evolution models and answer whether there is a reset in the chemical conditions of massive star-forming regions.

References

Alina, D. et al. (July 2020). "Large-scale magnetic field in the Monoceros OB-1 East molecular cloud". In: *arXiv e-prints*, arXiv:2007.15344, arXiv:2007.15344.

Alves, J., M. Lombardi, & C. J. Lada (Jan. 2007). "The mass function of dense molecular cores and the origin of the IMF". In: *A&A* 462.1, pp. L17–L21.

André, Ph. et al. (July 2010). "From filamentary clouds to prestellar cores to the stellar IMF: Initial highlights from the Herschel Gould Belt Survey". In: *A&A* 518, L102, p. L102.

Bally, John (Sept. 2016). "Protostellar Outflows". In: *ARA&A* 54, pp. 491–528.

Barnes, A. T. et al. (May 2021). "ALMA-IRDC: dense gas mass distribution from cloud to core scales". In: *MNRAS* 503.3, pp. 4601–4626.

Bertoldi, Frank & Christopher F. McKee (Aug. 1992). "Pressure-confined Clumps in Magnetized Molecular Clouds". In: *ApJ* 395, p. 140.

Beuther, H. (Jan. 2007). "Physics and chemistry of hot molecular cores". In: *Triggered Star Formation in a Turbulent ISM*. Ed. by Bruce G. Elmegreen & Jan Palous. Vol. 237, pp. 148–154.

Beuther, H. et al. (June 2007a). "Dust and gas emission in the prototypical hot core G29.96-0.02 at sub-arcsecond resolution". In: *A&A* 468.3, pp. 1045–1056.

Beuther, H. et al. (Oct. 2007b). "The 10^5 $L_\odot$ high-mass protostellar object IRAS 23151+5912". In: *A&A* 473.2, pp. 493–500.

Bohlin, R. C., B. D. Savage, & J. F. Drake (Aug. 1978). "A survey of interstellar H I from Lalpha absorption measurements. II." In: *ApJ* 224, pp. 132–142.

Bonnell, I. A. et al. (June 2001). “Accretion in stellar clusters and the initial mass function”. In: 324 (3), pp. 573–579.

Bonnell, I. A. et al. (May 2001). “Competitive accretion in embedded stellar clusters”. In: *MNRAS* 323.4, pp. 785–794.

Bonnell, Ian A. & Matthew R. Bate (July 2006). “Star formation through gravitational collapse and competitive accretion”. In: *MNRAS* 370.1, pp. 488–494.

Burkhart, Blakesley (June 2021). “Diagnosing Turbulence in the Neutral and Molecular Interstellar Medium of Galaxies”. In.

Butler, Michael J. & Jonathan C. Tan (May 2009). “Mid-Infrared Extinction Mapping of Infrared Dark Clouds: Probing the Initial Conditions for Massive Stars and Star Clusters”. In: *ApJ* 696.1, pp. 484–497.

– (July 2012). “Mid-infrared Extinction Mapping of Infrared Dark Clouds. II. The Structure of Massive Starless Cores and Clumps”. In: *ApJ* 754.1, 5, p. 5.

Carey, S. J. et al. (Jan. 2009). “MIPSGAL: A Survey of the Inner Galactic Plane at 24 and 70 μm”. In: *PASP* 121.875, p. 76.

Chakrabarti, Sonali & Sandip K. Chakrabarti (Feb. 2000). “Can DNA bases be produced during molecular cloud collapse?” In: *A&A* 354, pp. L6–L8.

Chandrasekhar, S. & E. Fermi (July 1953). “Magnetic Fields in Spiral Arms.” In: *ApJ* 118, p. 113.

Cheng, Yu et al. (Feb. 2018). “The Core Mass Function in the Massive Protocluster G286.21+0.17 Revealed by ALMA”. In: *ApJ* 853.2, 160, p. 160.

Chiappini, C., F. Matteucci, & R. Gratton (Mar. 1997). “The Chemical Evolution of the Galaxy: The Two-Infall Model”. In: *ApJ* 477.2, pp. 765–780.

Churchwell, Ed (Jan. 2002). “Ultra-Compact HII Regions and Massive Star Formation”. In: *ARA&A* 40, pp. 27–62.

Colzi, L. et al. (Aug. 2020). “Carbon isotopic fractionation in molecular clouds”. In: *A&A* 640, A51, A51.

Commerçon, B. et al. (Feb. 2022). “Discs and outflows in the early phases of massive star formation: Influence of magnetic fields and ambipolar diffusion”. In: *A&A* 658, A52, A52.

Condon, James J. & Scott M. Ransom (2016). *Essential Radio Astronomy*.

Cosentino, G. et al. (Dec. 2020). “SiO emission as a probe of cloud-cloud collisions in infrared dark clouds”. In: *MNRAS* 499.2, pp. 1666–1681.

Csengeri, T. et al. (Apr. 2017). "ALMA survey of massive cluster progenitors from ATLASGAL. Limited fragmentation at the early evolutionary stage of massive clumps". In: *A&A* 600, L10, p. L10.

Cyganowski, C. J. et al. (July 2017). "Simultaneous low- and high-mass star formation in a massive protocluster: ALMA observations of G11.92-0.61". In: *MNRAS* 468.3, pp. 3694–3708.

Devaraj, R. et al. (Apr. 2021). "Magnetic Fields and Star Formation around H II Regions: The S235 Complex". In: *ApJ* 911.2, 81, p. 81.

Egan, M. P. et al. (Feb. 1998). "A Population of Cold Cores in the Galactic Plane". In: *ApJL* 494.2, pp. L199–L202.

Fedriani, Rubén et al. (Jan. 2023). "The SOFIA Massive (SOMA) Star Formation Survey. IV. Isolated Protostars". In: *ApJ* 942.1, 7, p. 7.

Garrod, Robin T. (Mar. 2013). "A Three-phase Chemical Model of Hot Cores: The Formation of Glycine". In: *ApJ* 765.1, 60, p. 60.

Goldreich, P. & S. Sridhar (Jan. 1995). "Toward a Theory of Interstellar Turbulence. II. Strong Alfvenic Turbulence". In: *ApJ* 438, p. 763.

Gonzalez, Guillermo, Donald Brownlee, & Peter Ward (July 2001). "The Galactic Habitable Zone: Galactic Chemical Evolution". In: *ICARUS* 152.1, pp. 185–200.

Gorai, Prasanta et al. (Mar. 2023). "Astrochemical Diagnostics of the Isolated Massive Protostar G28.20-0.05". In: *arXiv e-prints*, arXiv:2303.02772, arXiv:2303.02772.

Heitsch, Fabian et al. (Nov. 2001). "Magnetic Field Diagnostics Based on Far-Infrared Polarimetry: Tests Using Numerical Simulations". In: *ApJ* 561.2, pp. 800–814.

Hernandez, Audra K. & Jonathan C. Tan (Aug. 2015). "The Giant Molecular Cloud Environments of Infrared Dark Clouds". In: *ApJ* 809.2, 154, p. 154.

Heyer, M., J. D. Soler, & B. Burkhart (Aug. 2020). "The relative orientation between the magnetic field and gradients of surface brightness within thin velocity slices of ^{12}CO and ^{13}CO emission from the Taurus molecular cloud". In: *MNRAS* 496.4, pp. 4546–4564.

Hillenbrand, Lynne A. & Lee W. Hartmann (Jan. 1998). "A Preliminary Study of the Orion Nebula Cluster Structure and Dynamics". In: *ApJ* 492.2, pp. 540–553.

Hoare, M. G. et al. (Jan. 2007). "Ultracompact Hii Regions and the Early Lives of Massive Stars". In: *Protostars and Planets V*. Ed. by Bo Reipurth, David Jewitt, & Klaus Keil, p. 181.

Hsu, Chia-Jung et al. (Mar. 2021). "Deuterium chemodynamics of massive pre-stellar cores". In: *MNRAS* 502.1, pp. 1104–1127.

Hu, Yue et al. (June 2019). "Magnetic field morphology in interstellar clouds with the velocity gradient technique". In: *Nature Astronomy* 3, pp. 776–782.

Inutsuka, Shu-ichiro et al. (Aug. 2015). "The formation and destruction of molecular clouds and galactic star formation. An origin for the cloud mass function and star formation efficiency". In: *A&A* 580, A49, A49.

Kainulainen, J. & J. C. Tan (Jan. 2013). "High-dynamic-range extinction mapping of infrared dark clouds. Dependence of density variance with sonic Mach number in molecular clouds". In: *A&A* 549, A53, A53.

Kirk, Helen & Philip C. Myers (Feb. 2011). "Young Stellar Groups and Their Most Massive Stars". In: *ApJ* 727.2, 64, p. 64.

Kirsanova, M. S. et al. (Aug. 2008). "Star formation around the HII region Sh2-235". In: *MNRAS* 388.2, pp. 729–736.

Kobayashi, Chiaki, Amanda I. Karakas, & Hideyuki Umeda (July 2011). "The evolution of isotope ratios in the Milky Way Galaxy". In: *Monthly Notices of the Royal Astronomical Society* 414 (4), pp. 3231–3250. ISSN: 00358711.

Könyves, V. et al. (Dec. 2015). "A census of dense cores in the Aquila cloud complex: SPIRE/PACS observations from the Herschel Gould Belt survey". In: *A&A* 584, A91, A91.

Krumholz, Mark R. (Sept. 2011). "Star Formation in Molecular Clouds". In: *XV Special Courses at the National Observatory of Rio de Janeiro*. Ed. by Eduardo Telles, Renato Dupke, & Daniela Lazzaro. Vol. 1386. American Institute of Physics Conference Series, pp. 9–57.

Kuffmeier, M. et al. (July 2020). "Linear dust polarization during the embedded phase of protostar formation. Synthetic observations of bridge structures". In: *A&A* 639, A137, A137.

Larson, R. B. (Mar. 1981). "Turbulence and star formation in molecular clouds." In: *MNRAS* 194, pp. 809–826.

Law, Chi-Yan et al. (Nov. 2022). "Isolated Massive Star Formation in G28.20-0.05". In: *ApJ* 939.2, 120, p. 120.

Lazarian, A. et al. (Sept. 2018). "Distribution of Velocity Gradient Orientations: Mapping Magnetization with the Velocity Gradient Technique". In: *ApJ* 865.1, 46, p. 46.

Li, H. B. et al. (Jan. 2014). "The Link Between Magnetic Fields and Cloud/Star Formation". In: *Protostars and Planets VI*. Ed. by Henrik Beuther et al., p. 101.

Lim, Wanggi et al. (Jan. 2016). "The Mass Surface Density Distribution of a High-Mass Protocluster forming from an IRDC and GMC". In: *American Astronomical Society Meeting Abstracts #227*. Vol. 227. American Astronomical Society Meeting Abstracts, 424.06, p. 424.06.

Liu, Junhao, Qizhou Zhang, & Keping Qiu (Sept. 2022). "Magnetic field properties in star formation: A review of their analysis methods and interpretation". In: *Frontiers in Astronomy and Space Sciences* 9, 943556, p. 943556.

Liu, Junhao et al. (June 2020). "Magnetic Fields in the Early Stages of Massive Star Formation as Revealed by ALMA". In: *ApJ* 895.2, 142, p. 142.

Liu, Mengyao et al. (Aug. 2018). "The Core Mass Function across Galactic Environments. II. Infrared Dark Cloud Clumps". In: *ApJ* 862.2, 105, p. 105.

Lu, Xing et al. (May 2022). "A massive Keplerian protostellar disk with flyby-induced spirals in the Central Molecular Zone". In: *Nature Astronomy* 6, pp. 837–843.

Matteucci, Francesca (Dec. 2021). "Modelling the chemical evolution of the Milky Way". In: *A&AR* 29.1, 5, p. 5.

McKee, Christopher F. & Eve C. Ostriker (Sept. 2007). "Theory of Star Formation". In: *ARA&A* 45.1, pp. 565–687.

McKee, Christopher F & Jonathan C Tan (Mar. 2003). "The Formation of Massive Stars from Turbulent Cores". In: 585 (2), pp. 850–871.

McKee, Christopher F. & Jonathan C. Tan (Mar. 2003). "The Formation of Massive Stars from Turbulent Cores". In: *ApJ* 585.2, pp. 850–871.

McMullin, J. P. et al. (Oct. 2007). "CASA Architecture and Applications". In: *Astronomical Data Analysis Software and Systems XVI*. Ed. by R. A. Shaw, F. Hill, & D. J. Bell. Vol. 376. Astronomical Society of the Pacific Conference Series, p. 127.

Moser, Emily et al. (July 2019). "The High-Mass Protostellar Population of a Massive Infrared Dark Cloud". In: *arXiv e-prints*, arXiv:1907.12560.

Motte, Frédérique, Sylvain Bontemps, & Fabien Louvet (2017). "High-Mass Star and Massive Cluster Formation in the Milky Way". In: *Annual Review of Astronomy and Astrophysics* December, pp. 1–42.

Motte, Frédérique, Sylvain Bontemps, & Fabien Louvet (Sept. 2018). "High-Mass Star and Massive Cluster Formation in the Milky Way". In: *ARA&A* 56, pp. 41–82.

Mouschovias, T. Ch. & Jr. Spitzer L. (Dec. 1976). "Note on the collapse of magnetic interstellar clouds." In: *ApJ* 210, p. 326.

Myers, Andrew T. et al. (Apr. 2013). "The Fragmentation of Magnetized, Massive Star-forming Cores with Radiative Feedback". In: *ApJ* 766.2, 97, p. 97.

Myers, Philip C. & Shantanu Basu (Aug. 2021). "Magnetic Properties of Star-forming Dense Cores". In: *ApJ* 917.1, 35, p. 35.

Nakano, T. & T. Nakamura (Jan. 1978). "Gravitational Instability of Magnetized Gaseous Disks 6". In: *PASJ* 30, pp. 671–680.

O'Neill, Theo J. et al. (July 2021). "The Core Mass Function across Galactic Environments. III. Massive Protoclusters". In: *ApJ* 916.1, 45, p. 45.

Ostriker, Eve C., James M. Stone, & Charles F. Gammie (Jan. 2001). "Density, Velocity, and Magnetic Field Structure in Turbulent Molecular Cloud Models". In: *ApJ* 546.2, pp. 980–1005.

Padoan, Paolo et al. (Oct. 2001). "Theoretical Models of Polarized Dust Emission from Protostellar Cores". In: *ApJ* 559.2, pp. 1005–1018.

Padoan, Paolo et al. (Sept. 2020). "The Origin of Massive Stars: The Inertial-inflow Model". In: *ApJ* 900.1, 82, p. 82.

Perault, M. et al. (Nov. 1996). "First ISOCAM images of the Milky Way." In: *A&A* 315, pp. L165–L168.

Pillai, T. et al. (Jan. 2015). "Magnetic Fields in High-mass Infrared Dark Clouds". In: *ApJ* 799.1, 74, p. 74.

Pontoppidan, Klaus M. & Sandra M. Blevins (Jan. 2014). "The chemistry of planet-forming regions is not interstellar". In: *Faraday Discussions* 168, p. 49.

Rathborne, J. M., J. M. Jackson, & R. Simon (Apr. 2006). "Infrared Dark Clouds: Precursors to Star Clusters". In: *ApJ* 641.1, pp. 389–405.

Reissl, S., S. Wolf, & D. Seifried (June 2014). "Tracing the ISM magnetic field morphology: the potential of multi-wavelength polarization measurements". In: *A&A* 566, A65, A65.

Reissl, S. et al. (July 2017). “The origin of dust polarization in molecular outflows”. In: *A&A* 603, A71, A71.

Rice, S. O. (Jan. 1944). “Mathematical Analysis of Random Noise”. In: *Bell System Technical Journal* 23, pp. 282–332.

Rodríguez, Luis F. (Jan. 2005). “Radio observations of ultracompact HII regions”. In: *Massive Star Birth: A Crossroads of Astrophysics*. Ed. by R. Cesaroni et al. Vol. 227, pp. 120–127.

Romano, Donatella (Dec. 2022). “The evolution of CNO elements in galaxies”. In: *A&AR* 30.1, 7, p. 7.

Romano, Donatella et al. (Dec. 2019). “The evolution of CNO isotopes: the impact of massive stellar rotators”. In: *Monthly Notices of the Royal Astronomical Society* 490 (2), pp. 2838–2854. ISSN: 0035-8711.

Rosen, Anna L. et al. (June 2020). “Zooming in on Individual Star Formation: Low- and High-Mass Stars”. In: *Space Science Reviews* 216 (4), p. 62. ISSN: 0038-6308.

Sanhueza, Patricio et al. (Dec. 2019). “The ALMA Survey of 70 μm Dark High-mass Clumps in Early Stages (ASHES). I. Pilot Survey: Clump Fragmentation”. In: *ApJ* 886.2, 102, p. 102.

Seifried, D. & S. Walch (Sept. 2015). “The impact of turbulence and magnetic field orientation on star-forming filaments”. In: *MNRAS* 452.3, pp. 2410–2422.

Seifried, D. et al. (May 2012). “Magnetic fields during the early stages of massive star formation - II. A generalized outflow criterion”. In: *MNRAS* 422.1, pp. 347–366.

Sewiło, M et al. (July 2008). “Internal Dynamics of the Hypercompact H II Region G28.20-0.04N”. In: 681 (1), pp. 350–354.

Shu, Frank H., Fred C. Adams, & Susana Lizano (Jan. 1987). “Star formation in molecular clouds: observation and theory.” In: *ARA&A* 25, pp. 23–81.

Simon, R. et al. (Dec. 2006). “The Characterization and Galactic Distribution of Infrared Dark Clouds”. In: *ApJ* 653.2, pp. 1325–1335.

Skalidis, Raphael & Konstantinos Tassis (Mar. 2021). “High-accuracy estimation of magnetic field strength in the interstellar medium from dust polarization”. In: *A&A* 647, A186, A186.

Snell, Ronald L. & Stanley E. Kurtz (2019). *Fundamentals of Radio Astronomy: Astrophysics (Series in Astronomy and Astrophysics)*.

Soam, Archana et al. (Sept. 2019). “Magnetic Fields in the Infrared Dark Cloud G34.43+0.24”. In: *ApJ* 883.1, 95, p. 95.

Sokolov, Vlas et al. (Oct. 2017). "Temperature structure and kinematics of the IRDC G035.39-00.33". In: *A&A* 606, A133, A133.

Tan, J. C. et al. (Jan. 2014). "Massive Star Formation". In: *Protostars and Planets VI*, p. 149.

Tan, Jonathan C et al. (Dec. 2013). "The Dynamics of Massive Starless Cores with ALMA". In: 779 (2), p. 96.

Tan, Jonathan C. et al. (Dec. 2013). "The Dynamics of Massive Starless Cores with ALMA". In: *ApJ* 779.2, 96, p. 96.

Tanaka, Kei E. I., Jonathan C. Tan, & Yichen Zhang (Jan. 2017). "The Impact of Feedback During Massive Star Formation by Core Accretion". In: *ApJ* 835.1, 32, p. 32.

Tang, Ya-Wen et al. (June 2019). "Gravity, Magnetic Field, and Turbulence: Relative Importance and Impact on Fragmentation in the Infrared Dark Cloud G34.43+00.24". In: *ApJ* 878.1, 10, p. 10.

Tinsley, B. M. (Jan. 1980). "Evolution of the Stars and Gas in Galaxies". In: *FCP* 5, pp. 287–388.

van der Tak, F. F. S. (Sept. 2004). "Hot Molecular Cores and High Mass Star Formation". In: *Star Formation at High Angular Resolution*. Ed. by Michael G. Burton, Ray Jayawardhana, & Tyler L. Bourke. Vol. 221, p. 59.

Ward-Thompson, Derek & Anthony P. Whitworth (2011). *An Introduction to Star Formation*. Cambridge University Press. ISBN: 9780511974021.

Wenger, Trey V. et al. (June 2021). "The Southern H II Region Discovery Survey. II. The Full Catalog". In: *ApJA* 254.2, 36, p. 36.

Wood, Douglas O. S. & Ed Churchwell (Apr. 1989). "The Morphologies and Physical Properties of Ultracompact H II Regions". In: *ApJA* 69, p. 831.

Wu, Benjamin et al. (May 2018). "Giant molecular cloud collisions as triggers of star formation. VI. Collision-induced turbulence". In: *PASJ* 70, S57, S57.

Xu, Duo, Chi-Yan Law, & Jonathan C. Tan (Jan. 2023). "Application of Convolutional Neural Networks to Predict Magnetic Fields' Directions in Turbulent Clouds". In: *ApJ* 942.2, 95, p. 95.

Yuen, Ka Ho & A. Lazarian (Mar. 2017). "Tracing Interstellar Magnetic Field Using Velocity Gradient Technique: Application to Atomic Hydrogen Data". In: *ApJL* 837.2, L24, p. L24.

Zinnecker, Hans & Harold W. Yorke (Sept. 2007). "Toward Understanding Massive Star Formation". In: *ARA&A* 45.1, pp. 481–563.